IMPROVEMENT AND VALIDATION OF MULTIYEAR AURORAL ANALYSIS TO CATEGORIZE SCINTILLATION EVENT LAYER

BY

BREANNA R. ENGLISH

Submitted in partial fulfillment of the
requirements for the degree of
Master of Science in Mechanical and Aerospace Engineering
in the Graduate College of the
Illinois Institute of Technology

Approved _______________
Adviser

Chicago, Illinois
December 2022

ACKNOWLEDGEMENT

This thesis would not have been possible without the enormous personal and professional support I have gotten from my advisor and committee chair Dr. Seebany Datta-Barua. Without her, I would not have even considered writing this thesis, so I would like to thank her again for believing in me and helping make this possible. I would also like to express my gratitude to Dr. Boris Pervan and Dr. Don Hampton for their wisdom and support. I have grown immensely as a researcher and a professional under their guidance. Additionally, I want to recognize my labmates for all their help, including restarting my lab computer and listening to my practice presentations. Special thanks also goes out to my family and friends, who listened to my woes and bought me food to get me through the hard times. Lastly, I would like to thank my girlfriend, who encouraged me to pursue research and believed in me and my work even when I doubted myself.

This research has made use of the Stellarium planetarium.

The material contained in this document is based upon work supported by a National Aeronautics and Space Administration (NASA) grant 80NSSC21K1354. Any opinions, findings, conclusions, or recommendations expressed in this material are those of the author and do not necessarily reflect the views of NASA. The support of the Illinois Space Grant Consortium under the auspices of the NASA Space Grant is greatly appreciated.

AUTHORSHIP STATEMENT

I, Breanna English, attest that the work in this thesis is substantially my own.

In accordance with the disciplinary norm of Mechanical and Aerospace Engineering (see IIT Faculty Handbook, Appendix S), the following collaborations occurred in the thesis:

Dr. Don Hampton (D.H.), of University of Alaska Fairbanks, Fairbanks AK, contributed the keogram and all-sky image data sets used for analysis, and their corresponding calibration methods.

David Stuart (D.S), of Illinois Institute of Technology, Chicago IL, contributed the original all-sky image and keogram analysis methodologies that are validated and analyzed in this work.

TABLE OF CONTENTS

LIST OF TABLES

LIST OF FIGURES

LIST OF SYMBOLS

Symbol	Definition
c	Coefficient of variation
S	All Sky Image (ASI) raw sensor data in units of camera counts
t	time
δ	GPS Satellite angular distance from the magnetic zenith at Poker Flat Research Range
λ	Wavelength
μ	Mean of a keogram scan line
$\rho_{630nm/428nm}$	Ratio of the 630 nm (red) calibrated ASI to the 428 nm (blue) calibrated ASI.
σ	Standard deviation of a keogram scan line

ABSTRACT

Ionospheric irregularities scintillate electromagnetic waves, such as Global Positioning System (GPS) signals, as they pass through the ionosphere, especially in auroral zones. A previous method was developed to determine which layer of the ionosphere these scintillation events occurred in by analyzing optical all sky images (ASI). The results of determining the ionospheric scattering layer using the ratio of 630 nm (red) intensity to 428 nm (blue) intensity were compared to a radar-based method of determining the scintillation layer, and it was found that the results disagreed.

In this work, the ASI method is critically analyzed to identify possible errors or sensitivities in the original method that might resolve the discrepancy. This is done by improving and validating the nighttime auroral cloud detection method by comparing to National Oceanic and Atmospheric Administration (NOAA) satellite cloud data. Then a sensitivity analysis is performed on the ASI method to determine which parameters of the method the results are sensitive to.

The keogram cloud detection method is improved by automating the selection of the keogram time points that are used to calculate a flat-field gain correction, and by calculating the flat field gain for each year rather than calculating it once and using it for all years of the study. Keogram cloud detection using the coefficient of variation is verified by comparing the keogram results to true sky conditions based on NOAA cloud mask data, and using detection theory to determine the optimal coefficient of variation threshold. We find that the ideal keogram threshold was 0.37 producing a disagreement rate of 22.4%.

The ASI image analysis criteria tested are: the ASI azimuth and elevation mapping files, the magnetic zenith limit, the number of pixels of the ASI that are being analyzed, the duration of the scintillation event that is analyzed, and the red-

to-blue ratio threshold. It is found that only changing the red-to-blue ratio threshold has a significant effect on the ASI method, with the red-to-blue ratio that minimizes the number of misattributed layers found to be 1.43.

CHAPTER 1
INTRODUCTION

Aurorae occur at the northern and southern poles of the Earth, aurora borealis and aurora australis, respectively, and are colloquially known as the northern and southern lights. Solar wind, plasma composed of charged particles, is emitted from the sun and strikes Earth's magnetic field. While some of the particles are deflected around the Earth, some flow along the magnetic field lines towards the poles and into the ionosphere. The ionosphere is a region of Earth's atmosphere that is dominated by ionized particles, where plasma dynamics dominate the region's behavior [1]. Optical emissions result from the chemical interactions between solar wind particles and the particles in the Earth's ionosphere.

Aurorae are of great scientific interest due to the fact that they are evidence of the connection between space and Earth. The ionosphere ranges from 50-2000 km above the Earth's surface [1]. Figure 1.1 shows the electron density profile of the ionosphere and how the ionosphere layers are defined based on the electron density peaks. The D layer of the ionosphere is the lowest region, with the lowest electron density, roughly below 90 km altitude, and exists only in the daytime. The E region is the next higher layer with the first electron density peak, approximately 90 - 150 km. The F region has the next and largest electron density peak, around 150 - 600 km altitude.

In addition to the visual effects of aurorae, they are also a form of space weather that impact electromagnetic waves as they pass through. This has been seen extensively with Global Positioning System (GPS) technology in the form of scintillation events, which occur when a GPS signal goes through irregularities causing phase and/or amplitude fluctuations of the original signal, impeding the accuracy of GPS navigation. Ionospheric irregularities are the electron structuring and density gradi-

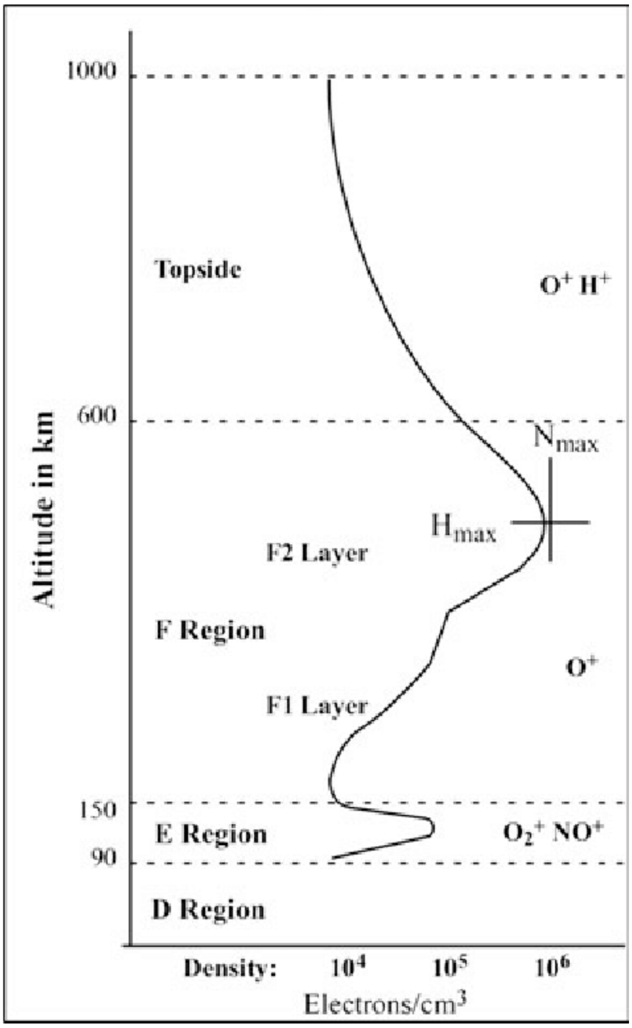

Figure 1.1. Electron density profile of the ionosphere as the altitude increases and the corresponding ionosphere layers from [2].

ents in the ionosphere [1]. Ionospheric irregularities cause diffraction and refraction in electromagnetic signals [3].

For investigating the aurorae and the processes associated with them, wide field-of-view optical images of the night sky, all sky images (ASI), and keograms from a meridian spectrograph are collected at Poker Flat Research Range near Fairbanks, Alaska. Previous work analyzed the ASI to try to determine in which layer of the ionosphere scintillation events that were recorded had occurred, the E or F layer [4]. The keograms [4] were used to find cloud-free intervals, as clouds obstruct the view of the sky and render the all sky images unusable for this analysis.

The objective of this thesis is to improve and validate the keogram cloud detection method, and improve the previously-developed method in [5] for scintillation event layer categorization using all sky images. These objectives are met in the contributions of the thesis.

The contributions of this thesis are:

1. **Contribution 1: Validation of automated nighttime cloud detection using keograms while aurora is present.** I improved the flat-field correction method by automating the process of selecting time points that are used in the calculation of the flat field gain, and calculating the flat field gain for each year rather than using a single calibration for multiple years. I introduced an intensity threshold to remove dark sky intervals from both the cloud detection and ASI analysis, since keogram cloud detection will not work during dark sky times. I verified the keogram cloud detection method, based on the coefficient of variation of the keogram over viewing angle, by using NOAA cloud mask data as a truth reference, and selected the optimal coefficient of variation threshold using detection theory.

2. **Contribution 2: All sky image spectral analysis sensitivity analysis.** The ASI orientation calibration files being used were verified to be correct for 2014-2018 all sky images. I investigated the magnetic zenith range within which the GPS scintillating signal is required to lie for a layer determination to be made, the number of ASI pixels surrounding the GPS satellite position in the sky, the red-to-blue intensity ratio as a function of time during a scintillation event, and the red-to-blue ratio to ensure that the method implemented was correct. There was little to no sensitivity to the magnetic zenith limit, the

number of pixels analyzed, and the duration of the scintillation event analyzed. An optimal red-to-blue ratio threshold was found to be 1.43. The original study was also expanded from only 2014-2015 to 2014-2018.

CHAPTER 2
BACKGROUND

2.1 Scintillation

Scintillation is the rapid phase and/or amplitude fluctuation of a received electromagnetic wave. Scintillation has been observed to affect GPS signals, meaning the received signal has quick amplitude, phase, or both, variations, compared to the signal that was sent from the satellite. Scintillation occurs when signals pass through ionospheric irregularities, such as electron density structures and density gradients, causing the signal to refract and diffract. Scintillations are an active area of research as the disturbance of the GPS signals can cause signal loss or small navigation errors that can be hard to detect. Scintillating GPS signals also provide a method of probing the ionosphere with existing infrastructure.

Figure 2.1 depicts a satellite sending a signal that passes through the ionosphere and encounters ionospheric irregularities, represented by the light blue cloud shapes. The irregularities cause the signal to refract and diffract [3], causing the signal that is received by receivers on the ground to have a rapidly varying amplitude and/or phase. A set of GPS receivers over some baseline distances of up to a kilometer may have similar fluctuations that are time-shifted, which can be leveraged for GPS-based sensing of the irregularities.

GPS signals are transmitted at frequencies L1 (1575.42 MHz) and L2C (1227.60 MHz). Phase scintillation is quantified by the standard deviation of the phase σ_ϕ, and amplitude scintillation by a normalized amplitude standard deviation index S_4, or both may occur [6]. One of the areas of research involving scintillation is to identify in which ionospheric layer they are occurring, E-layer or F-layer. The layers have different compositions and behaviors which could be causing the irregularities that lead

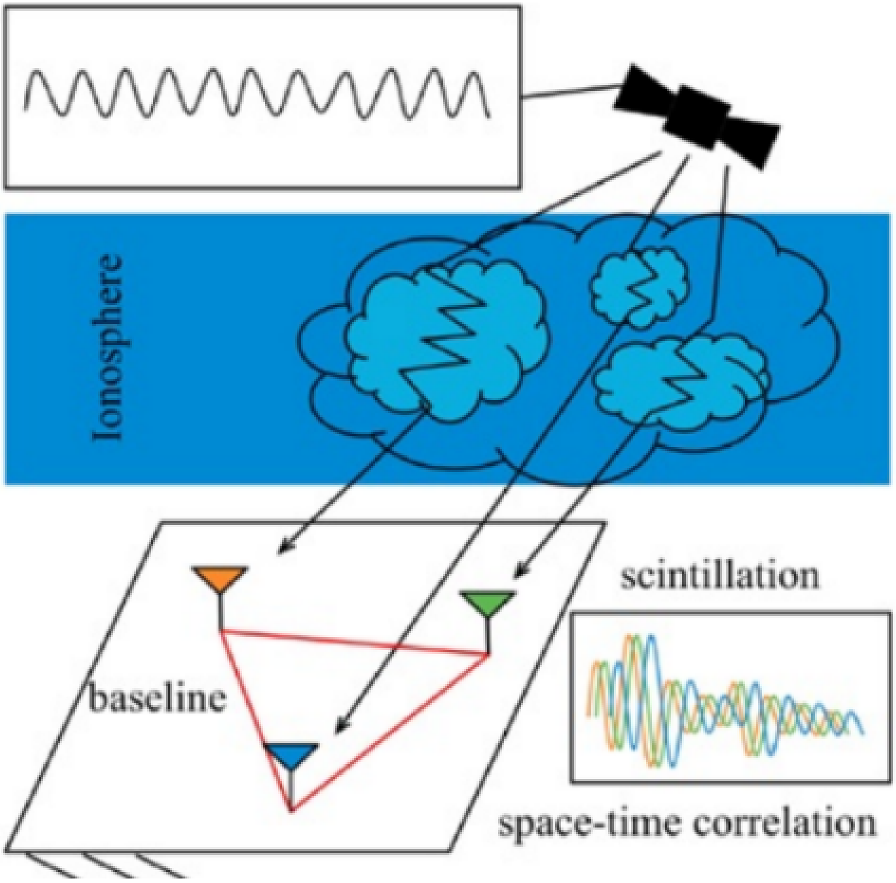

Figure 2.1. Depiction of a signal from a satellite encountering ionospheric irregularities and being scintillated [6].

to scintillations. The E-layer has higher neutral densities which can affect plasma dynamics through collisions, while the F-layer has sparse neutrals and a lower rate of collisions [1].

2.2 Aurora

Aurora are the optical emissions seen at latitudes around the magnetic poles as charged particles precipitate from the magnetosphere down along field lines into the atmosphere. The color of the aurora can be used to gain insight to what is happening in the ionosphere. Figure 2.2 illustrates the colors emitted by altitude in the ionosphere. The ionospheric layers can also be characterized by the neutral particles that inhabit them. The neutral species that the F layer lies within is mostly atomic oxygen, and the E layer is mostly inhabited by molecular nitrogen [1].

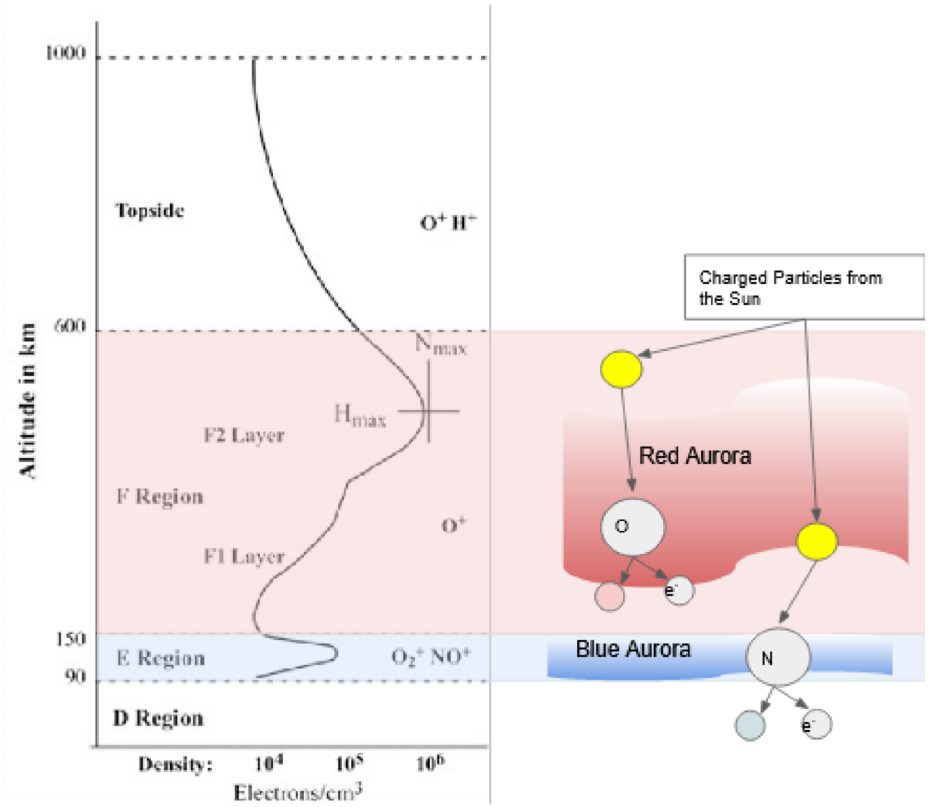

Figure 2.2. Layers of the ionosphere with the corresponding auroral emissions that would be produced from charged particles interacting with the neutral particles in the respective layers, modified from [2].

Charged particles from the sun interact with the neutral particles in the ionosphere in the auroral zones and produce emissions of specific wavelengths depending on the particles they interact with. When an energetic particle interacts with atomic oxygen, it produces an electron and a photon of wavelength 630 nm, red [1]. When a charged particle interacts with the molecular nitrogen, it produces an electron and a photon of wavelength 428 nm, blue [1]. The optical light seen from the aurora can be used to determine which layer of the ionosphere has the highest electron production rate. Knowing which layer has the highest electron production rate can be used to determine which layer is causing signal scintillation.

Since scintillation is caused by ionospheric irregularities, the ionospheric layer with the highest electron production rate might be assumed to be where these signal scintillations are occurring. If the aurora is producing more 630 nm red light, there are more electrons being produced in the F layer, and the scintillation events are probably occurring in the F layer. Conversely, if there is more 428 nm blue light, the scintillations are probably occurring in the E layer.

2.3 Poker Flat Research Range

Poker Flat Research Range (PFRR) is located in Fairbanks, Alaska. PFRR has various instruments for investigating aurorae, the ionosphere, and scintillation: the Scintillation Auroral GPS Array (SAGA), Poker Flat Incoherent Scatter Radar (PFISR), All Sky Images (ASI), and a meridian spectrograph, which produces keograms. Figure 2.3 shows a map of PFRR and the locations of the different instruments available.

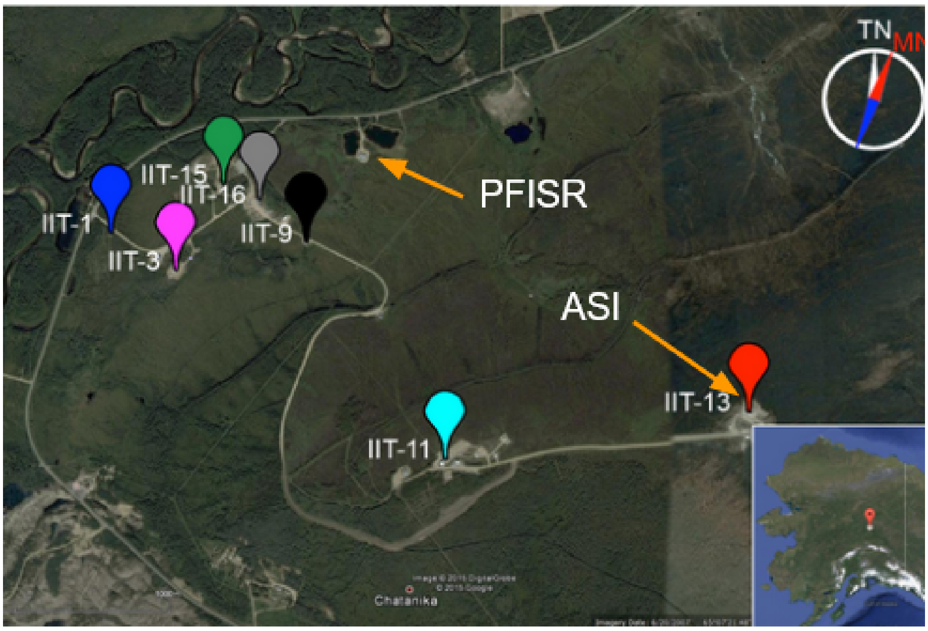

Figure 2.3. Map of Poker Flat Research Range with the SAGA receivers, PFISR, and ASI camera locations shown.

The Scintillation Auroral GPS Array (SAGA) is an array of GPS receivers at Poker Flat Research Range in Alaska that receive GPS signals from the satellites that are passing overhead [6]. This array is used to detect when a GPS signal has been scintillated. Fig. 2.3 shows the location of all of the SAGA receivers at PFRR, each receiver named “IIT-#”. The data collected from the receivers were previously analyzed to identify a list of scintillation events [7]. The scintillation event list encompasses all events detected by SAGA from 2014-2019. The list gives the start time, end time, GPS frequency, and which GPS satellite the scintillation signal came from. This scintillation event list used in the ASI method to know when the scintillation events were occurring and which satellite the signal was coming from, so we could determine which pixel of the ASI to analyze to determine the scintillation vent layer.

PFISR is a radar that makes electron density measurements as function of time and altitude. Previously [7] used PFISR to hypothesize, based on the altitude of the maximum plasma density, which ionospheric layer (E or F) might contain the irregularities that caused each of the scintillation events in the list. In that work, a slight majority of the scintillation events were found to be in the E layer in 2014, and the percentage became increasingly E layer as the solar cycle declined to solar minimum, by 2019.

Even though a majority of events were found to be in the E layer based on PFISR [7], using maximum density is an imperfect assumption. All-sky images are an alternative data set for determining which layer the signal was scintillated in, based on the altitude of maximum ionization rate. The ratio of red-to-blue intensities from the theory of a Maxwellian particle population traveling along the field line, corresponds to the ionization rate profile. Initial results by [5] determining the irregularity layer based on ASI disagreed with the determination for those same events based on PFISR; the majority of events seemed to be in the F region, based on a red-to-blue ratio of 0.5 chosen from theory. This E versus F discrepancy between PFISR and ASI layer determination is the motivation for this work.

Section reviews the prior work of [5], whose methods are investigated in detail in this work. One of the first steps is removal of images during cloudy times, because auroral light is too blurred. Keograms are collected by a meridian spectrograph; they are used in Chapter 3 for cloud detection. Section 3.1.2 gives a more detailed description of the meridian spectrograph and keograms. Section 4.1.2 gives more information on the ASIs as they are used in this work.

2.4 Detection Theory

Both contributions rely on concepts in detection theory. Detection theory is used to determine the effectiveness of a method to detect the presence of some signal by comparing the methods results to the truth [8]. This is done by simply calculating how often the method has correctly detects the presence of the signal (Hit), correctly identifies the absence of the signal (Correct Rejection), incorrectly detects the signal when there is none (False Alarm), and fails to detect the signal when it is present (Miss).

The hit and correct rejection categories are achieved when the detection method result and the true result agree, referred to as correct decisions. The false alarm and missed detection categories are the events for which the method prediction and the true results disagree, in this work called the “mislabeled events.” For an ideal detector, 100% of the detections would be correct decisions. A detection matrix, used to find the missed detection and false alarm rates, is shown in a simple 2-by-2 matrix in Fig. 2.4.

When evaluating and tuning a detection method, detection theory can be used to determine the best detection thresholds to set. The detection threshold is a numerical value for the metric that differentiates between a present signal and an absent signal. By using the detection theory and looping through various threshold

		Method Prediction Results	
		Signal Present	Signal Absent
True Results	Signal Present	Hit	Miss
	Signal Absent	False Alarm	Correct Rejection

Figure 2.4. Matrix showing the detection theory category of comparing a method to the true results.

possibilities, the best threshold can be identified.

The “best” threshold can depend on the method or on requirements on the detector performance. For most methods, the best threshold is the one with the lowest mislabeled rate. In some cases, there is a limit to how high the false alarm rate can be. These situations may be ones where false alarms are more detrimental than misses. There may be some cases where the opposite is true. Detection theory is a tool that can be used to improve detection methods, but the application of the tool depends on the requirements of system needing the detection method.

In this work, detection theory is used to determine the best keogram coefficient of variation cloud detection threshold using NOAA cloud mask data as truth. It is also used to determine what the ideal red-to-blue ratio threshold would be to get the ASI spectral analysis results to be in agreement with PFISR results. In both cases, the best detection threshold is the one with the lowest number of mislabeled events.

2.5 ASI Spectral Analysis Prior Work

The multiyear automated analysis of auroral images method was originally developed by David Stuart [5]. This section will summarize the method as originally developed, before being investigated and further adjusted in the contribution sections.

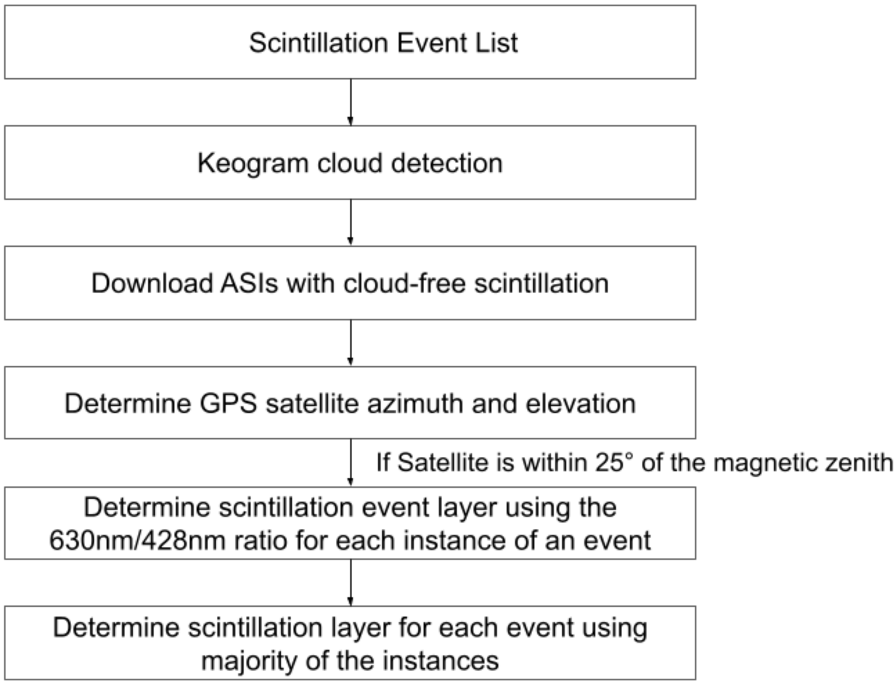

Figure 2.5. Method of analyzing ASIs to determine scintillation event layer from [5].

Figure 2.5 gives an overview of the ASI analysis method that was developed in [5]. First, the scintillation event list generated from SAGA is downloaded. Then keograms are used to determine which events are cloud-free. Clouds scatter light, blurring the images and making the data contained in those images unusable for spectral analysis. Then the cloud-free ASIs are downloaded and the GPS azimuth and elevation angle during the cloud-free scintillation times are calculated using the GPS almanacs from [9]. If a satellite is within 25° of the magnetic zenith, those ASIs can be used to determine the scintillation event layer using the ratio of the 630 nm emission to the 428 nm emission intensity. Charged particles are confined to travel along a magnetic field line. All particles on one field line are part of the same particle population. The magnetic zenith direction is the one that points up along the local magnetic field line. If the line of sight from the SAGA receivers to the scintillating satellite (and likewise from the line of sight of the camera to the satellite) is not aligned enough with the magnetic field line, as given by the magnetic zenith direction, then the theory that allows us to use the red-to-blue ratio to compute characteristic energy and thus the layer, no longer holds true. The magnetic zenith limit is in place to ensure that the assumption of a single particle population holds, for using the ratio in a way that is consistent with Maxwellian distribution theory. The method is described in more detail in the next subsections 2.5.1 and 2.5.2.

2.5.1 Prior Work: Keogram Cloud Detection. Keograms are the images that are used to determine which times are cloud-free. When clouds are present over aurora in a keogram, the cloud smears the light coming from the aurora.

The initial keogram cloud detection method is shown in Figure 2.6. First, all of the keograms for the years of interest are downloaded from [4]. The keograms are then processed to convert them from raw sensor data to photon flux and to remove noise in the data.

After downloading, each keogram is converted from the raw data in units of camera counts to photon flux in Rayleighs by multiplying by the calibration factor, which is unique to each wavelength. Then the keograms are trimmed to remove excess sunlight from the times near dusk/dawn, and regions near the horizon. The dusk/dawn sunlight in the keograms over saturate the images and make it hard to analyze the auroral light in the middle of the night.

The keogram spectrograph makes a second measurement, the background keogram, by filtering at a nearby wavelength. Subtracting this background keogram removes noise due to light pollution and some keogram sensor bias.

Then a flat field correction-like step is applied to remove noise due to variations in the keogram sensors. The flat field correction method uses manually selected keogram snapshots that are as uniformly lit as possible to reconstruct the flat field gain. The flat field gain is then used to correct the images.

The calibrated and flat field corrected keograms are used to determine when clouds are present using the test statistic coefficient of variation. The coefficient of variation describes how much spatial variation there is at each time point of a keogram. It uses the fact that clouds scatter light uniformly, so when clouds are present, the keogram snapshot will look uniformly lit. The lower the coefficient of variation is, the more likely there are clouds present. Higher values mean that there are no clouds present scattering the light.

The coefficient of variation c for a wavelength λ is calculated using Eq. 2.1, which is the standard deviation of the keogram scan lines divided by the mean over all viewing angles. The cloud detection cut-offs were selected manually by visually inspecting 557.7 nm and 630.0 nm keograms. The original decision procedure and thresholds are shown in Figure 2.6. If the c_{557nm} is greater than or equal to 0.25, than the time point is cloud-free. If not, but the c_{630nm} is greater than or equal to 0.4, then it is still cloud-free. If the c_λ is less than both of those thresholds, then the time epoch is determined to be cloudy and should not be used for ASI analysis.

$$c_\lambda(t) = \frac{\sigma_\lambda(t)}{\mu_\lambda(t)} \tag{2.1}$$

With the cloudy and cloud-free times found using the keograms, only the all sky images during cloud-free times are used in the spectral analysis process.

2.5.2 Prior Work: All Sky Image Layer Determination.

Given the list of scintillation events, there are three conditions that must be met for the analysis to continue. There must be a scintillation event, there must be a

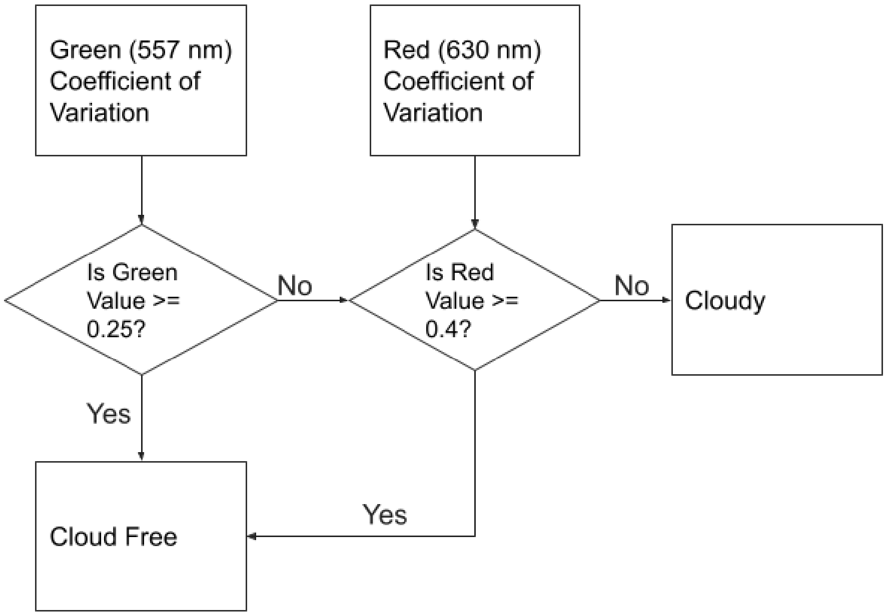

Figure 2.6. Method of determining cloud-free and cloudy times using the coefficient of variation.

triplet set of ASIs available during the event time, and the event must the cloud-free. The first condition is met using the scintillation event list. The third condition is met using the keogram cloud detection method outlined above. The second condition is met by comparing a list of the available ASI from Poker Flat Research Range [4] to the provided list of scintillation events.

The ASIs of the events meeting those 3 conditions are downloaded onto the local computer and calibrated. The azimuth and elevation of the GPS satellite that sent the scintillating signal is found using daily GPS Yuma almanacs [9]. Column-integrated auroral analysis used to categorize ionosphere layer [10] requires viewing near the magnetic zenith. The satellite must be within 25° of the magnetic zenith. The satellite pixel location on the ASI is found using the ASI calibration files. The calibration files show the azimuth and elevation associated with each pixel of an ASI. Using the GPS azimuth and elevation and the calibration files, the pixel associated with the scintillation signal at each time point is determined to be the one with the smallest angle difference between the satellite and the pixel.

Scintillation event categorization is done based on the auroral theory that provides the relation between observed constituent emissions and electron characteristic energy, α, which is used to estimate auroral height [10]. A red to blue (630nm/428nm) ratio ρ of 0.5 is used based on these theories. The irregularity layers are categorized by:

$$\text{if } \rho_{630/428} <= 0.5\text{, E-region irregularity instant}$$
$$\text{if } \rho_{630/428} > 0.5\text{, F-region irregularity instant}$$

ASIs are taken in red-green-blue ordered triplets at a cadence of 12.5 s. Since the threshold uses the red-to-blue ratio, the triplets are reordered to be green-blue-red in order to reduce the delay between the red and blue ASIs.

The final event layer categorization is determined by majority vote of the individual layer categorizations over the entire scintillation event duration. If there is a tie between E and F layer, the categorization is determined to be E layer.

The results of the original ASI analysis method were then compared to PFISR results for 2014-2015. The results from [5] using this method are shown in Table 2.1. From the provided scintillation event list, a majority of the events were phase scintillations. Of the few events that were amplitude or amplitude-phase shifts, none of them met the conditions to be analyzed by the ASI spectral analysis method. Therefore, all of the results in Table 2.1 are phase scintillation events.

Table 2.1 shows the numbers and percentages of layer categorization using the ASI method compared to the PFISR method. The ASI method determines the irregularity layer to be E region for 22.5% of the events and F layer for the majority, or 77.5% of the events. Ignoring the events that were either missing radar data (50.5%)

or ambiguous (5.5%), a the PFISR classification of events is E layer twice as often as it is F layer (30% vs. 14%).

Table 2.1. ASI Categorized Events Compared to PFISR Results from [5]

Scintillation Category	ASI E-Layer	ASI F-Layer	PFISR E-Layer	PFISR F-Layer	PFISR Ambiguous	PFISR Missing Data
2014 L1	36	107	60	30	12	41
	25.2%	74.8%	42.0%	21.0%	8.4%	28.7%
2015 L1	23	76	16	1	2	80
	23.2%	76.8%	16.2%	1.0%	2.0%	80.8%
2014 L2	13	52	25	19	6	15
	20.0%	80.0%	38.5%	29.2%	9.2%	2.1%
2015 L2	10	47	8	1	0	48
	17.5%	82.5%	14.0%	1.8%	0.0%	84.2%
Total	82	282	109	51	20	184
	22.5%	77.5%	29.9%	14.0%	5.5%	50.5%

These results shown in [5] raised the questions of whether underlying physics, different experimental methods, or choices in the ASI methodology create the difference in the ASI and PFISR method results. Fundamentally, ASI measures active ionization, while radar measures electron density. Scintillation is driven by around 100 m scale irregularities in electron density gradients. The PFISR beam at the magnetic zenith presents a challenge as the active ionosphere layer is not constant for the entire sky at the same time, assuming the spectral analysis method is correct.

The disagreement between these two methods seen in Table 2.1 is the motivation for this work. To ensure those results are correct, many aspects of the ASI analysis method are analyzed in this work to determine if the disagreement might be due to invalid assumptions or choices in the spectral analysis methodology.

CHAPTER 3

AUTOMATED NIGHTTIME CLOUD DETECTION USING KEOGRAMS WHILE AURORA IS PRESENT

This chapter describes the work done to improve the keogram-based cloud detection method. Fig. 3.1 shows flowcharts of the original method used to detect clouds (left) and the method after improvements were implemented. In addition the improved method is validated using an independent data source of satellite imagery as truth.

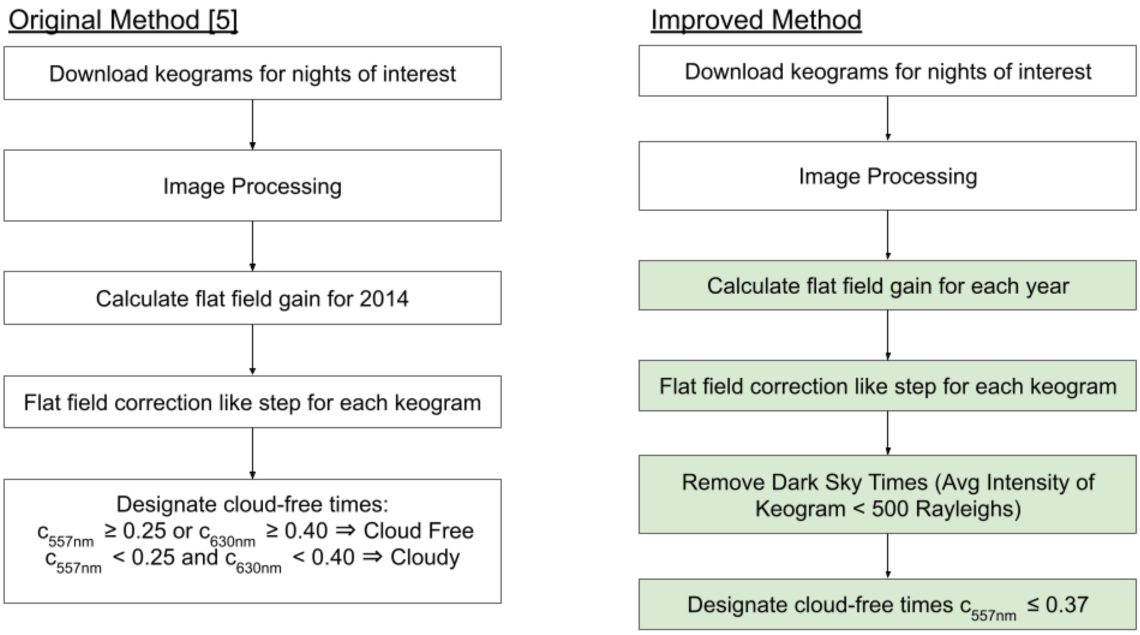

Figure 3.1. Flowcharts showing the original method used to detect clouds using keograms developed in [5] and the method after the improvements are implemented. The improvements are highlighted in green on the improved method flowchart.

3.1 Data

3.1.1 National Oceanic and Atmospheric Administration Cloud Mask Data.

National Oceanic and Atmospheric Association (NOAA) have extensive weather data available for public use. The data set used in this study is the Advanced Very High Resolution Radiometer (AVHRR) and High-resolution Infra-Red Sounder

(HIRS) Pathfinder Atmospheres Extended (PATMOS-x) Climate Data Record (CDR). The AVHRR+HIRS Cloud Properties - PATMOS-x CDR provides data for multiple cloud properties, brightness, and temperatures collected by the AVHRR and HIRS instruments on board the NASA Polar Operational Environmental Satellites (POES) and European MetOp platforms [11].

The cloud property used in this thesis is cloud mask. Cloud mask describes how cloudy it was at a given latitude, longitude, and time on a scale of 0-3; 0: clear, 1: probably clear, 2: probably cloudy, 3: strong cloud. In this work, only the data with cloud mask 0 and 3 are used to reduce error due to uncertainty. This data is used to verify the keogram cloud detection method and fine tune the distinction threshold between cloudy/cloud-free in keograms.

3.1.2 Meridian Spectrograph. The meridian spectrograph takes a one pixel wide scan line image of the sky from the northern horizon to the southern horizon passing through local zenith. Figure 3.2 shows a schematic of the meridian spectrograph setup. The meridian spectrograph takes images in 6 different wavelengths cycling over all of them at a 12.5 second cadence: 428.7 nm, 486.1 nm, 520 nm, 557.7 nm, 630 nm, 670 nm. The meridian spectrograph produces keograms at each wavelength for each night the spectrograph is operational.

A keogram is a time sequence of one-dimensional images taken over the course of a night. A keogram is an image including each 12.5 second scan line for the entirety of the night in one of the six wavelengths. A 557nm keogram is shown in Fig. 3.3a. Keograms are the images that are used to determine whether or not the sky is cloudy.

3.2 Automated Flat Field Correction

Before using keograms to determine the cloudy and cloud-free intervals, they have to be flat field corrected (FFC). The original flat field correction method is

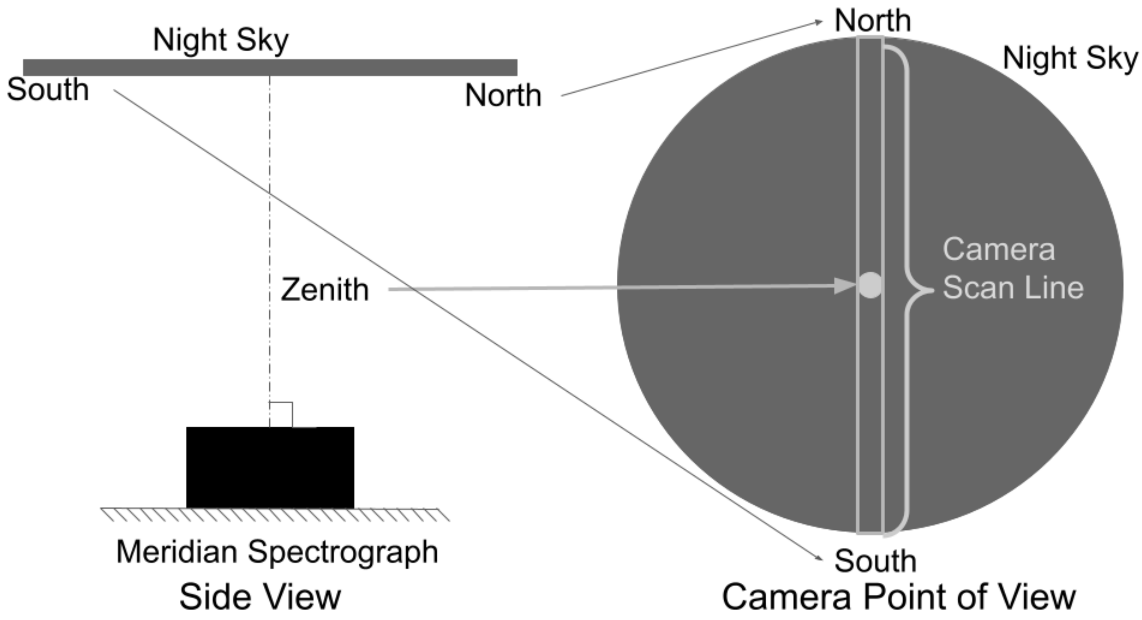

Figure 3.2. Schematic of keogram imaging system. The left shows a side view of a meridian spectrograph looking up local zenith and the left shows a view of the night sky from the perspective of a camera as the meridian spectrograph takes one-pixel-wide scans from horizon to horizon through local zenith.

described in [5]. That method calculated a flat field gain (FFG) from one manually selected time interval to correct the keograms. That FFG was then used to correct all the keograms for the entirety of the study, at the time 2014-2015.

Over time, instrument sensors can vary, meaning a flat field gain calculated using one day will not necessarily be accurate for data years into the future. Now that the study is being extended past 2014 and 2015, it is important to create an automated method of calculating the flat field gain and apply it to every year of the study.

Keogram times that are as uniformly lit as possible are used to calculate an accurate flat field gain. The coefficient of variation is a measure of how much variation there is at a keogram time point, or how uniformly lit that time point is. This makes the coefficient of variation a good metric to use in finding mostly uniformly lit keogram time points.

Using the coefficient of variation, the method of determining uniformly lit keogram time points can be automated. Time points with a coefficient of variation c less than or equal to 0.15 are used to calculate the flat field gain. Figure 3.3 shows the new method of calculating the flat field gain being applied to January 1, 2014. The flat field gain shown in Figure 3.3c is used to correct the keograms in 2014.

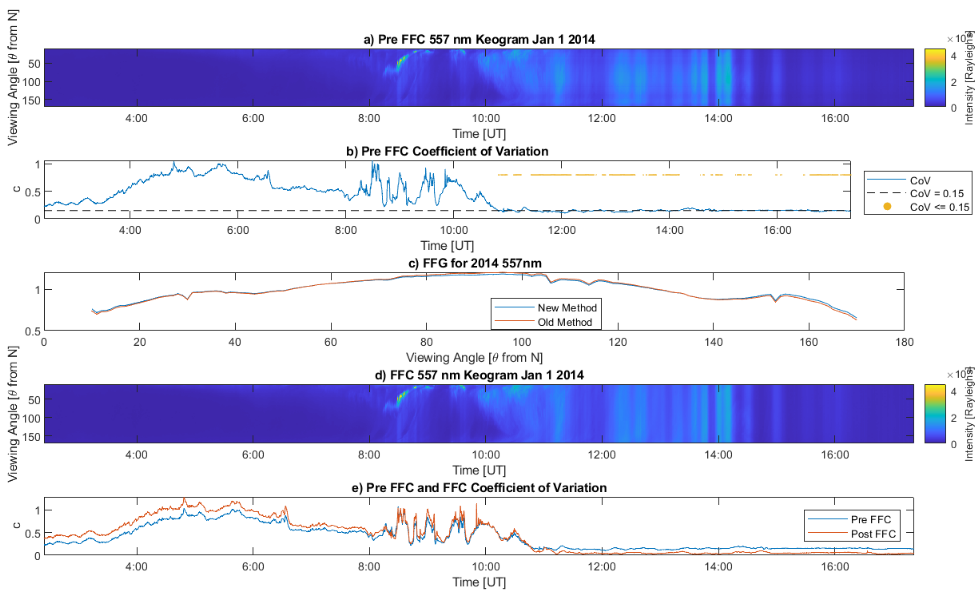

Figure 3.3. New method of determining the time points to calculate the flat field gain. (a) Calibrated but not flat-field-corrected keogram of 1 Jan 2014 with the corresponding sample (b) coefficient of variation with the time points where the c is less than or equal to 0.15, (c) flat field gain using the old method and this new method, (d) flat-field-corrected keogram using the flat field gain obtained by the new method, and (e) the coefficient of variation before and after flat field correction.

Figure 3.3 shows the calibrated pre-FFC keogram in 3.3a, the coefficient of variation of the calibrated keogram in 3.3b, with the coefficient of variation $c = 0.15$ dashed line and the times where the calibrated coefficient of variation is less than or equal to 0.15 as yellow dots in 3.3b. Figure 3.3c shows the flat field gain calculated using the old method described in [5], and the new flat field gain calculated from the time intervals having coefficient of variation $c \leq 0.15$. Figure 3.3d shows the flat field corrected keogram using the new flat field gain, and 3.3e shows the coefficient of variation of the calibrated pre flat field corrected keogram in 3.3a and the flat field corrected keogram. After flat field correction, not only are the camera variations removed, but the coefficient of variation of cloud-free times have a higher coefficient of variation, and the cloudy times have an even lower coefficient of variation, when comparing the pre and post flat field corrected coefficient of variation values. Flat-field correction makes cloudy and cloud-free times more distinguishable.

3.3 Dark Sky Intervals in Keograms

The coefficient of variation is the test metric that is used to distinguish between cloudy and cloud-free sky times. The coefficient of variation, in Eq. 2.1, is the sample standard deviation of the keogram divided by its mean over all viewing angles at one epoch. Figure 3.4 shows the flat field corrected keogram and the three observed sky conditions outlined: dark sky in interval 1, cloud-free with aurora present in interval 2, and cloudy with aurora present in interval 3.

Interval 1 identified in Figure 3.4a corresponds to a dark sky with no aurora. A plot of the intensity as a function of elevation at an example instant identified is shown in Fig. 3.4b. The intensities are uniformly low. A histogram of these intensities over all angles at this instant is shown in Fig. 3.4c. It has a small sample mean and small sample standard deviation.

Interval 2 identified in Fig. 3.4a contains a segment of an auroral band in the northern part of the sky. For an example time, the intensity as a function of viewing angle is shown in Fig. 3.4d, consisting of one narrow region of high intensity at the viewing angle to the aurora. The sky is clear because we can see the narrow angular extent of the aurora. The histogram is shown in Fig. 3.4e, and there are clear outliers

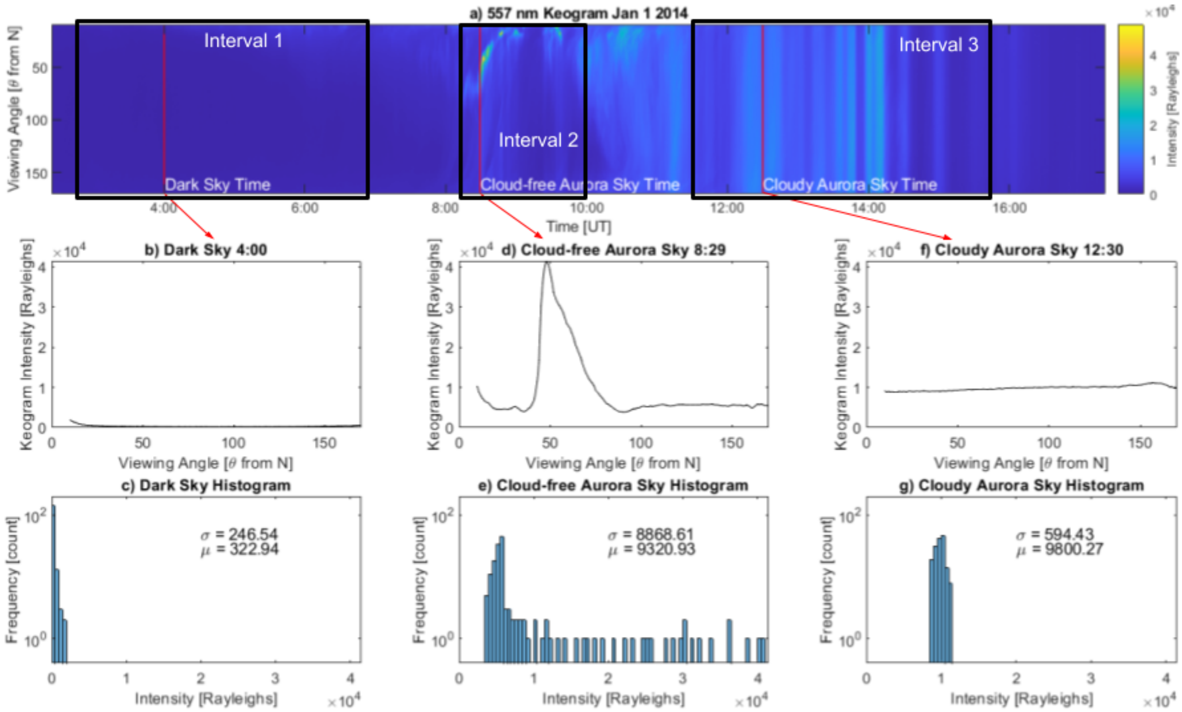

Figure 3.4. (a) Keogram for Jan 01 2014 for 557 nm wavelength with three sky conditions highlighted, (1) Dark sky, no aurora present (2) Cloud-free aurora time, and (3) Cloudy aurora time. The red lines in each interval are example time points that are expanded on in the following plots. (b) keogram intensity along the viewing angle for the dark sky example scan line (c) histogram of keogram intensity for the dark sky example (d) keogram intensity along the viewing angle for the cloud-free aurora time (e) the histogram of the keogram intensity of the cloud-free aurora time (f) keogram intensity along the viewing angle for the cloudy aurora time and (g) the histogram of the keogram intensity during the cloudy aurora time.

at the intensities corresponding to the auroral emission.

The interval 3 of Fig. 3.4a corresponds to a period during which there are aurorae, but the presence of clouds has possibly dimmed but, more importantly, also scattered the auroral light, smearing the intensities spatially to give a uniform appearance at all viewing angles, as shown in Fig. 3.4f. As a result, the distribution of keogram intensities in Fig. 3.4g is narrowly clustered around a non-zero mean.

Cloud cover has the effect of blurring the auroral light in the keogram. A commonly used image processing concept is useful here. Images taken are often post-processed to reduce noise or smooth out other unwanted effects by filtering. The mathematical process of filtering is given by convolution, which for a 1D image in θ can be written as:

$$(f * g)(\theta) \equiv \int f(\alpha)g(\theta - \alpha)d\alpha \tag{3.1}$$

In this operation, g is the kernel, or filter, that modifies the original signal f. In the language of image processing, clouds in the sky have a kernel g that, convolved with the light sources that would otherwise be present in a cloud-free keogram, produces a smoothed set of intensities received at the ground. Clouds between the the auroral source and the imager have the effect of smoothing out the intensities spatially, and effectively act as an imaging filter.

However, if there is no light source to be blurred, the cloud kernel has little effect. The distribution of a dark clear sky would be indistinguishable from that of a dark cloudy sky. For this reason we exclude the dark sky keogram intervals, such as Interval 1, from consideration. We do this by setting a minimum mean value of the samples which must be exceeded. The 557.7 nm keograms must have a mean intensity of at least 500 Rayleighs for there to be considered aurora present and usable for cloud detection.

3.4 Keogram Cloud Detection Verification

3.4.1 Method. The original cloud detection method used the 557 nm and 630 nm thresholds categorizing cloudy or cloud-free time points based on visual inspection of the keograms coefficient and variation. Going forward, only the 557 nm keograms will be used for cloud detection. The keogram cloud detection method and the coefficient of variation detection metric is compared against the NOAA AVHRR+HIRS Cloud Properties - PATMOS-x Climate Data Record (CDR) Cloud Mask Data in order to verify that the method is valid, and find the optimal threshold.

Within the CDR, the cloud mask is an index describing how cloudy the sky is at a given geographic latitude, geographic longitude, and time, on a scale of 0-3 as follows: 0: clear, 1: probably clear, 2: probably cloudy, 3: strong cloud. An example of the cloud mask data over Alaska is shown in Fig. 3.5. This data is used to train and test the keogram cloud detection method.

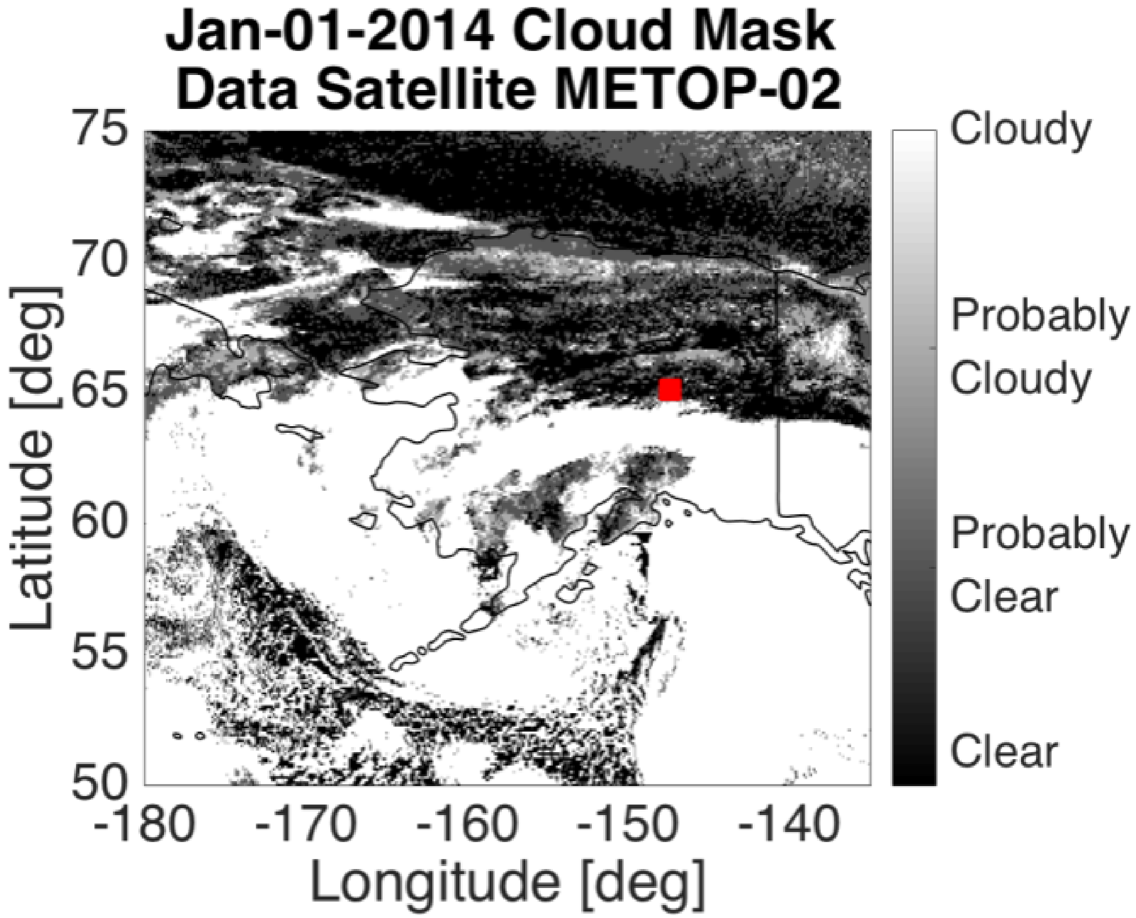

Figure 3.5. NOAA cloud mask data over Alaska with Poker Flat Research Range marked with a red square.

Detection theory is used to compare the NOAA cloud mask data and the keogram cloud detection results with NOAA cloud mask data acting as the true results and keogram cloud detection acting as the prediction method. Keogram cloud detection is defined as when the coefficient of variation is below a set threshold. When the coefficient of variation is above the threshold, clouds are not present. When NOAA cloud mask = 3, clouds are detected, and when the cloud mask = 0, clouds are not detected. Figure 2.4 is redone to represent the process of using detection theory with keogram and cloud mask data in Fig. 3.6. In this case, the goal will be to optimize the keogram coefficient of variation threshold such that the overall disagreement rate between the two methods is as low as possible.

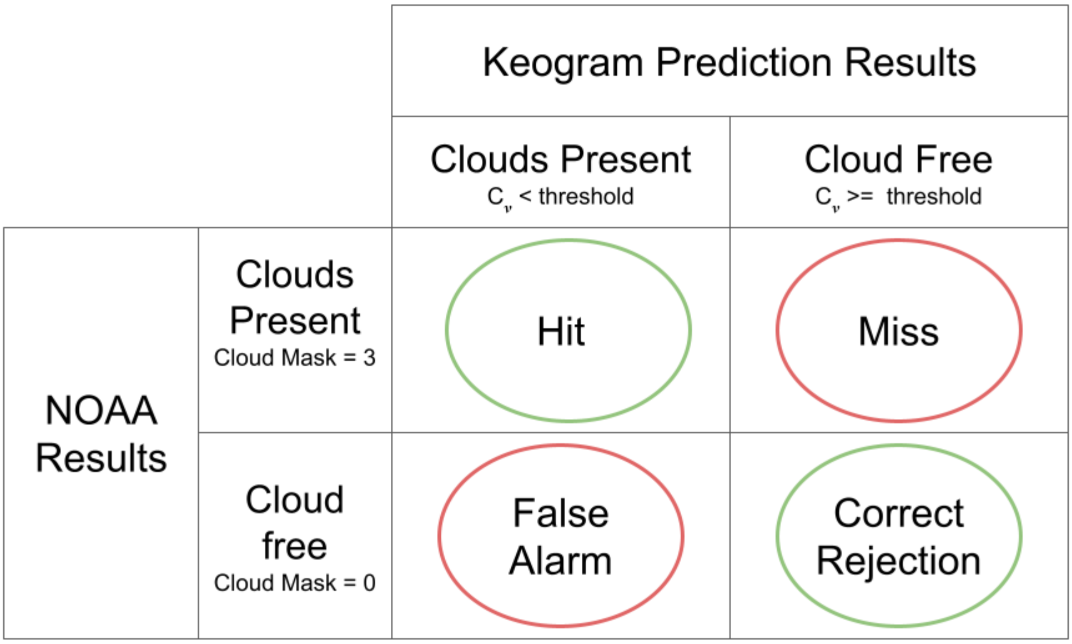

Figure 3.6. Detection theory matrix applied to using NOAA cloud mask data to verify the keogram cloud detection method.

The years 2014-2017 are used in this test. The even years, 2014 and 2016, are used as training data to determine the optimal thresholds, and the odd years, 2015 and 2017, are used as testing data to ensure the results from the training data are repeatable and accurate. Before being used in the validation test, all of the keograms are calibrated using the method described in [5], and the new flat field correction method.

Provisional cloud mask files, available daily for 2014-2017, are used. From each CDR cloud mask file, the times, cloud mask, and latitude and longitude of points within 8 km of Poker Flat Research Range are saved.

For each NOAA data point, we determine the keogram 557.7 nm snapshot that is closest in time and at most within 20 s of the time the keogram data was taken, since keogram images are taken at 12.5-s intervals. The NOAA data and the corresponding keogram data are then saved in a separate table. If there is more than one NOAA data point within 12.5 s of the same keogram timestamp, the NOAA pixel that is geographically closest to to PFRR is used, so that there was only one NOAA data point to one keogram data point.

Each keogram and cloud mask pair are categorized into one of four groups: 1) the keogram-derived coefficient of variation c and NOAA cloud categorization both indicate cloud-free conditions; 2) the keogram and NOAA cloud categorization both indicate cloudy; 3) the keogram categorization is cloud-free but the NOAA categorization says the sky is cloudy (missed detection by our method); and 4) the keogram categorization is cloudy and the NOAA categorization cloud-free (false alarm by our method). The NOAA categorization is determined from the cloud mask variable, corresponding to 0 when cloud-free, and 3 when cloudy. Only events that are either strongly cloudy (cloud mask 3) or strongly clear (mask 0) are used. The keogram cloud categorization is determined from the coefficient of variation at that timestamp being either less than the threshold (cloudy) or greater than or equal to the threshold (cloud-free).

With the training data of all keograms and cloud masks in 2014 and 2016, the objective is to find a threshold with the lowest percent of mislabeled events (missed detections and false alarms). The percent of mislabeled events is computed for 2014 and 2016 for thresholds on the coefficient of variation starting from 0.01 increasing by increments of 0.01 to 1.

The original method of cloud detection used both 630 nm and 557 nm keograms with thresholds of 0.4 and 0.25, respectively, as described in the flowchart in Fig. 2.6. First I will show the detection performance rates of the original method, compared to the NOAA cloud mask "truth." Then I will show the optimal combination of thresholds to use with the combination of red and green. I will show the performance rates are comparable to using only 557 nm coefficient of variation.

3.4.2 Results.

The results showing the keogram coefficient of variation performance as a detector using the original thresholds of 557 nm = 0.25 and 630 nm = 0.4 (set before comparing the keogram method to externally referenced truth) are shown in Table 3.1. The 'threshold' columns of the table are the thresholds that were used to determine if the events are cloudy or cloud-free using the keogram method. The 'total # of events' column are the number of events where there was NOAA cloud mask data within 8 km of Poker Flat Research Range and within 12.5 seconds of keogram data. The '# of total strong' are the number of the total number of events where NOAA cloud mask is strong cloudy (3) a or strong clear (0). The number of 'aurora present' events are the number of total strong events that also have an average intensity above 500 Rayleighs. The 'aurora present' events are the ones used to determine the optimal keogram cloud detection threshold (the denominator used for calculating percentages). The percent of events mislabeled with the original method is about 24% for the training data, and 30% for the testing data.

I analyzed mislabeling rates to find the optimal thresholds for the original method, of using 557 nm and 630 nm wavelengths sequentially, to determine cloud presence. The results are shown in Fig. 3.7. From the training data in Fig. 3.7a, the thresholds that produced the lowest number of mislabeled events are a 557 nm threshold of 0.5, with a 630 nm threshold of 0.4 or 0.5. Out of these two sets of

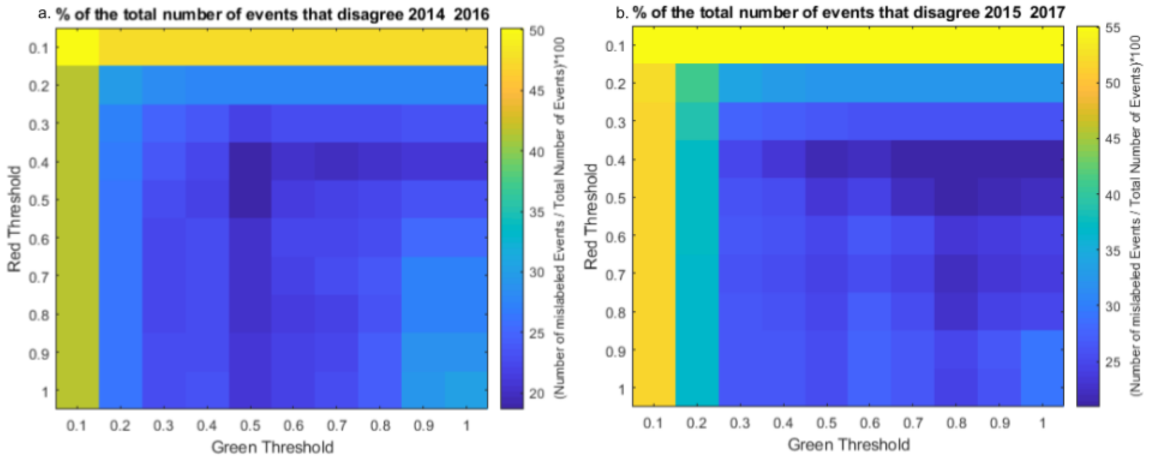

Figure 3.7. (a) Percentage of events mislabeled (color) for 2014 and 2016 events using thresholds starting from 0.1 to 1 with steps of 0.1 using both 630 nm and 557 nm wavelengths. (b) Percentage of events mislabeled (color) for 2015 and 2017 events using 557 nm and 630 nm thresholds 0.1 to 1 with steps of 0.1

thresholds that produced the lowest percent of events from the training data, the threshold of 0.5 for 557 nm and threshold 0.4 for 630 nm produce the lowest number of mislabeled events in the testing data as seen in Fig. 3.7b, although it is not the global minimum. The detector performance using the optimal thresholds of 0.5 (green) and 0.4 (red) are listed in Table 3.1. The mislabeled event rate drops by several percent for both the training data and the testing data, relative to the original method.

Next I tested a simpler cloud detection method that uses only the 557 nm keogram. The percentage of mislabeled events as a function of the coefficient of variation threshold for the training data is graphed in Fig. 3.8. The graph shows that the greenline threshold with the lowest percent of events that are mislabeled is 0.51, with about 20.7% of events mislabeled. The results of using the threshold of 0.51 on the even years (the training events), is shown in Table 3.2. Comparing the percent of mislabeled events using the 630 nm and 557 nm method (Table 3.1) to just the 557 nm method, we see that they are just a couple percent different. Since the 557 nm method is simpler, going forward I use the 557-nm-only cloud detection method,

Table 3.1. The detection results from the events in 2014 and 2016, and 2015 and 2017 using both 630 nm and 557 nm wavelengths (the original method of the flowchart in Fig. 2.6).

Years	Red Threshold	Green Threshold	Total # Events	Total # Strong	Aurora Present	Percent Matching	Correct Rejection	Hit	Percent Mislabeled	Miss	False Alarm
2014 and 2016	0.4	0.25	794	434	295	75.6	36.9	38.6	24.4	22.7	1.7
2015 and 2017	0.4	0.25	529	265	196	70.4	31.6	38.8	29.6	25.5	4.1
2014 and 2016	0.4	0.5	794	434	295	81.4	32.5	48.8	18.6	12.5	6.1
2015 and 2017	0.4	0.5	529	265	196	78.1	26.5	51.5	21.9	12.8	9.2

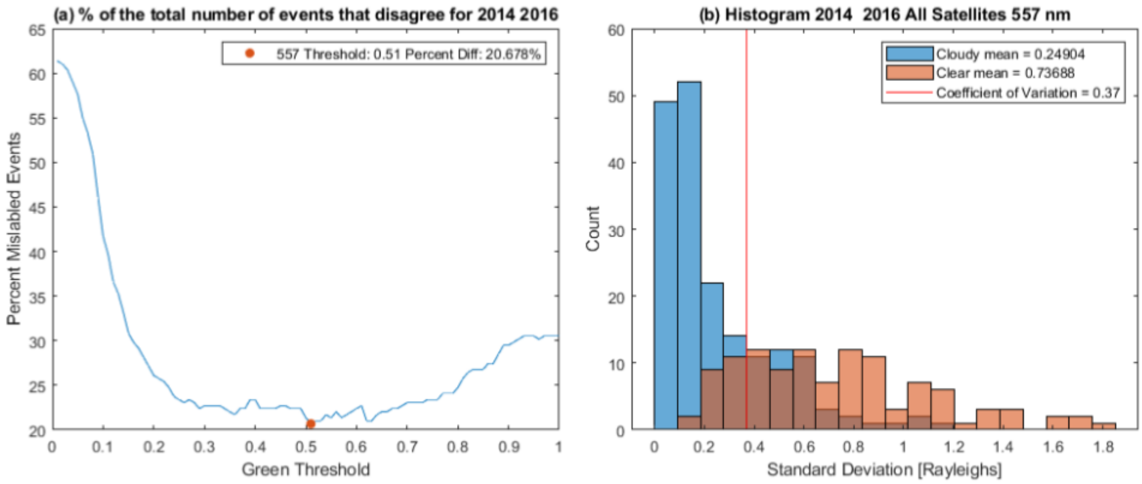

Figure 3.8. (a) Results from comparing 2014 and 2016 events using thresholds starting from 0.01 to 1 with steps of 0.01. The thresholds that produce the lowest mislabeled are highlighted with their mislabeled percentages shown in the legend. (b) Histogram of the cloudy and cloud-free NOAA categorized events and their respective keogram coefficients of variations.

rather than the originally proposed 557 nm and 630 nm cloud detection method.

The results of using the green-only method with the 0.51 threshold on the testing data of 2015 and 2017 are shown in Table 3.3, with 25% of the events in that data set mislabeled. To check how close the 0.51 threshold is to optimal for the testing data, I tested each threshold for 2015 and 2017 from 0.01 to 1 by 0.01; the results are plotted in Fig. 3.9a. The corresponding histograms of the coefficient of variation for cloudy and cloudless conditions are shown in Fig. 3.9b.

Running the test on 2015 and 2017 produce an ideal coefficient of variation of 0.37 with a disagreement rate of 24.0%. Comparing the percent mislabeled vs coefficient of variation threshold graphs of the even and odd years, Fig. 3.8a and Fig. 3.9a respectively, it can be seen that the odd years produce results with a sharper

Table 3.2. The detection results from the events in 2014 and 2016 for coefficient of variation thresholds 0.37 and 0.51.

Threshold	Total # Events	Total # Strong	Aurora Present	Percent Matching	Correct Rejection	Hit	Percent Mislabeled	Miss	False Alarm
0.37	794	434	295	77.6	31.2	46.4	22.4	14.9	7.5
0.51	794	434	295	79.3	26.1	53.2	20.7	8.1	12.5

Table 3.3. The detection results from the events in 2015 and 2017 for thresholds 0.37 and 0.51.

Threshold	Total # Events	Total # Strong	Aurora Present	Percent Matching	Correct Rejection	Hit	Percent Mislabeled	Miss	False Alarm
0.37	529	265	196	76.0	26.5	49.5	24.0	14.8	9.2
0.51	529	265	196	75.0	20.9	54.1	25.0	10.2	14.8

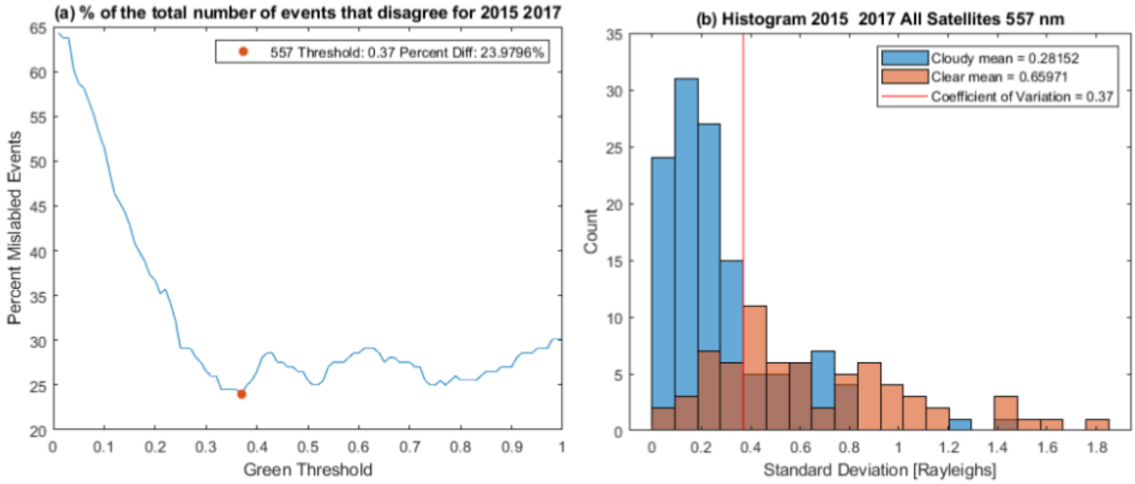

Figure 3.9. (a) Results from comparing 2015 and 2017 events using thresholds starting from 0.01 to 1 with steps of 0.01. The thresholds that produced the lowest mislabeled were highlighted with their mislabeled percentages shown in the legend. (b) Histogram of the cloudy and cloud-free NOAA categorized events and their respective keogram coefficients of variations.

minimum, whereas the even years have a shallow between 0.25 and 0.65, showing that almost any threshold in that range would produce similar results. The coefficient of variation results for 0.37 are also shown in Tables 3.2 and 3.3 for the training years and testing years, respectively. Using the 0.37 threshold on the even set of data produces a disagreement rate of 22.4%, only a 2% difference from the ideal threshold of 0.51. Since almost any coefficient of variation threshold in the shallow produces similar results and the odd year has a more distinct ideal threshold, the threshold of 0.37 for the 557 nm keogram will be used to detect clouds for the rest of this thesis.

CHAPTER 4

ALL SKY IMAGE SPECTRAL CLASSIFICATION ANALYSIS

The original ASI irregularity layer classification in Table 2.1 show that there is a big discrepancy between the ASI spectral analysis method and the PFISR method. This chapter investigates possible inconsistencies in the original spectral analysis method to see if there are any changes that need to be made to this method that might make it more aligned with the PFISR results. A flow chart of the new method is shown in Fig. 4.1. The changes that were made in the keogram process are highlighted in green, and were discussed in the previous chapter. The parts of the ASI analysis method that were investigated in this chapter are highlighted in yellow.

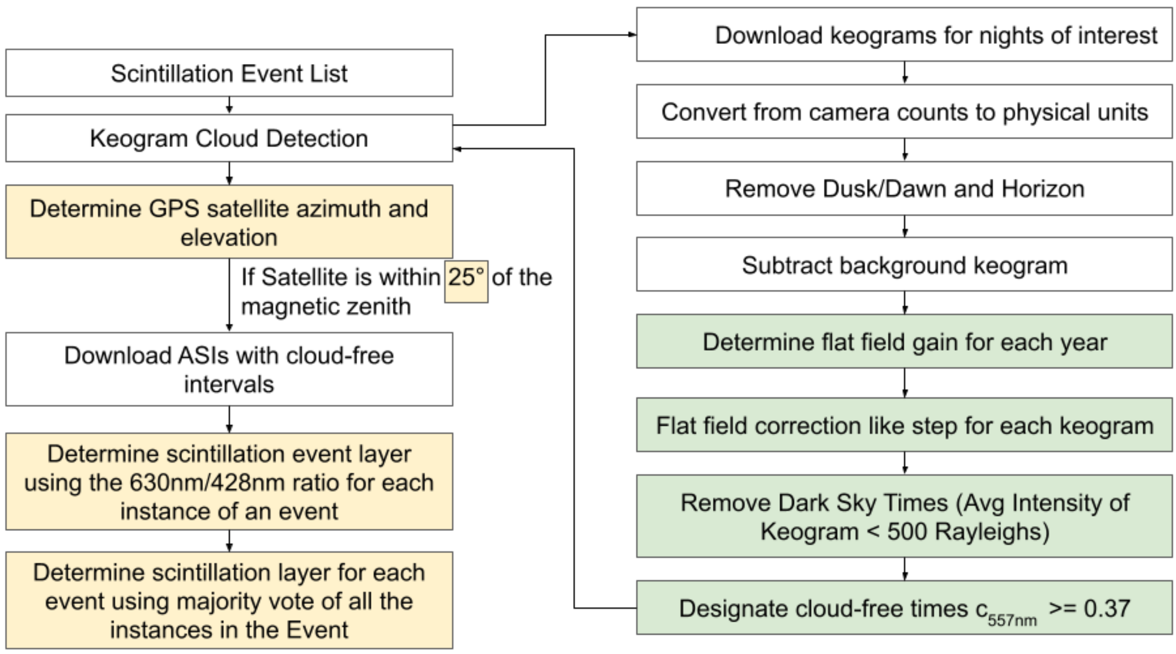

Figure 4.1. ASI spectral analysis method flow chart. The changes that were made from the original method are highlighted in green and the parts that were sensitivity analyzed are highlighted in yellow.

There was a change made to the order of the ASI analysis method as well, which can be seen by comparing Fig. 2.5 to the left half of Fig. 4.1: I moved the calculation of the GPS satellite azimuth and elevation to determine whether a scintillation event occurs near magnetic zenith to occur before downloading the ASIs. This reduces the amount of storage space needed on the computer for data and time, as only the images that are ultimately used in the layer analysis are downloaded.

When the spectral analysis method was originally developed, there were some constants and thresholds that were initially set. Some of those constants may need to be adjusted after further analysis into the effect they have on the final results. The goal of this section is to test how these thresholds affect the results and if there are better thresholds that could be set to bring the results closer to PFISR. If any of the thresholds need to be changed, we also want a sense of what the reason is. First we verify if the images' azimuth and elevation mappings are correct and consistent over the years investigated, 2018-2018. Then four different sensitivities are analyzed: the magnetic zenith range, the number of ASI pixels near the GPS scintillating satellite analyzed, the length of time of the scintillation event being analyzed, and the red-to-blue ratio threshold.

4.1 Data

4.1.1 PFISR electron densities.

PFISR, Poker Flat Incoherent Scatter Radar, takes electron density measurements as a function of time and altitude. An example of the PFISR data is shown in Figure 4.2. The solid vertical lines mark the scintillation time intervals of PRNs 25 and 29 as detected by SAGA. The dashed vertical lines mark the scintillation event detected for PRN 31. The horizontal line at 195 km divides the altitudes sensed by two different radar pulse types: above 195 km the long pulse is used and below 195 km the alternating code measurements are used [12]. With PFISR, the scattering layer causing scintillation is hypothesized to be the altitude with the electron density peak during the scintillation event, which in the case of Figure 4.2 is E layer [12].

The PFISR results for each scintillation event are provided in the overall scintillation event list [7]. The results of the original ASI method were compared to the PFISR layer method, and the resolving the discrepancy motivates this thesis. In this chapter, PFISR is used as a “truth” reference, for testing the ASI method threshold.

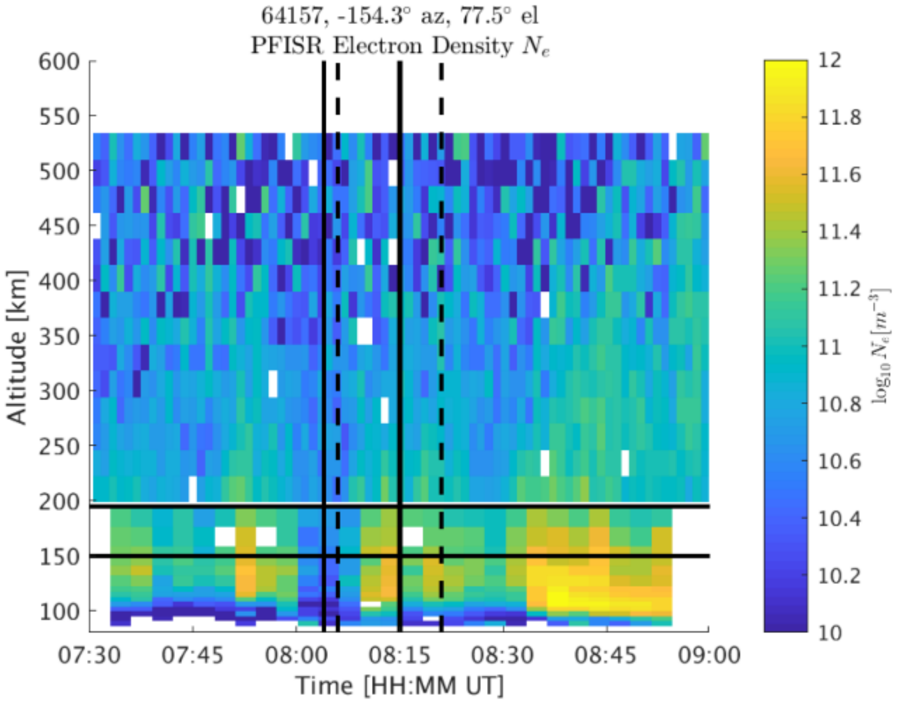

Figure 4.2. PFISR electron density measurements in magnetic zenith direction, March 18, 2015 7:30-9:00 UTC, plotted following the method of [12]. Peak density for 08:06 UTC is seen in the E-region.

4.1.2 All Sky Images.

All sky images (ASIs) are two-dimensional images from a camera whose field-of-view spans from horizon to horizon. ASIs are analyzed to determine the scintillation event layer. All sky images are taken with the all sky camera at Poker Flat Research Range. The camera takes images in 6 wavelengths at a ∼12.5 s cadence: 428.7 nm (blue), 486.1 nm, 520 nm, 557.7 nm (green), 630.0 nm (red), and 670 nm. In this chapter, only the 428 nm (blue) and 630 nm (red) all sky images are used. Fig. 4.3a shows what you would see looking up at the night sky from PFRR, and in Fig. 4.3b, the corresponding (1) blue, (2) red, and (3) green all sky images taken using the all sky camera. The processing and calibration, including conversions from camera counts to intensities, in can be found in [5]. In this chapter, surveys are conducted using ASIs that are cloud-free during scintillation events that occurred 2014-2018 based on the database of events identified by [7]. While the scintillation event database spans 2014-2019, the keograms in 2019 [13] could not be verified visually, so no cloud detection and subsequent ASI analysis is done in this work for those events. ASIs from select dates between 2014 and 2018 are used in Section 4.2. The sensitivity studies in Section 4.3 and the updated all-sky image layer determination in Section 4.1.2 use all the scintillation events that have cloud-free ASIs 2014-2018.

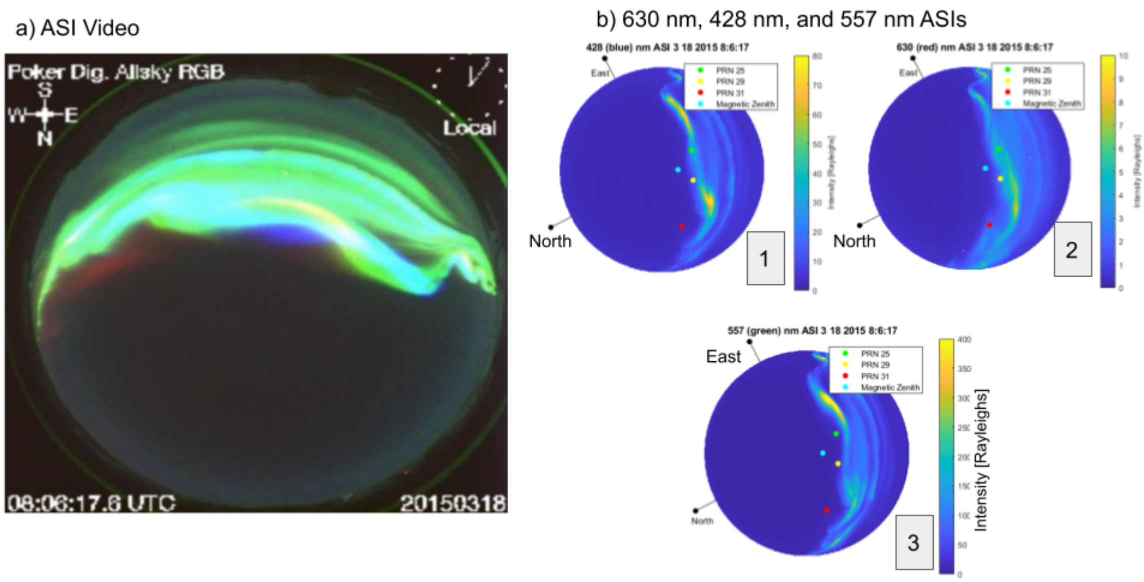

Figure 4.3. a) ASI video, what you would see looking up at the location of the all sky camera b) corresponding 630 nm, 428 nm, and 557 nm ASIs. Intensity is in kiloRayleighs (kR).

4.2 Image Rotation Check

When running the original spectral analysis, there was a significant drop in the percent of events that were being analyzed due to the magnetic zenith limit.

This can be seen in Table 4.1, which lists by year from 2014-2018, the number of scintillation events, the percent of those that are cloud-free using the original cloud-detection method, and the percent of the cloud-free subset that are within 25 degrees of magnetic zenith. This is the percent of the events that were cloud-free and within the magnetic zenith range. The percentage decreases significantly after 2015. The camera was relocated at PFRR sometime in 2015-2016 so it was possible that the rotation of the camera after being moved was not corrected. This would mean that the azimuth calibration file used to determine the orientation of the ASI is incorrect for files after the camera move. It would also indicate that the selection of pixels from which to compute the red-to-blue ratio were not selected correctly.

Table 4.1. ASI Spectral Analysis Results Original Method for L1 type Scintillation

Year	Scintillation Events	Percent Cloud Free	Subset Percent Magnetic Zenith	E Layer	F Layer
2014	844	41.7%	34.4%	28.1%	71.9%
2015	1179	18.6%	34.2%	21.3%	78.7%
2016	208	46.4%	18.9%	37.0%	63.0%
2017	92	69.6%	14.1%	100.0%	0.0%
2018	343	38.2%	8.4%	100.0%	0.0%

The moon is bright and easy to identify on the ASIs on clear nights. To check that the image azimuth/elevation calibration files are correct for all years, the files are used to determine the moon's azimuth and elevation for instants in 2014 to 2018. The angles are compared against the true values of the moon's azimuth and elevation. The true values are found using Stellarium, an astronomy application [14].

The first step is choosing the ASIs where the moon is very apparent. The moon oversaturates the ASIs and causes the maximum values for the images to go over 10,000 kR, as seen in the example in Fig. 4.4a. ASIs with a moon present have maximum intensities over 10,000 kR. These images are then visually inspected to make sure that the moon is easily identified. One ASI per night with an apparent moon was chosen.

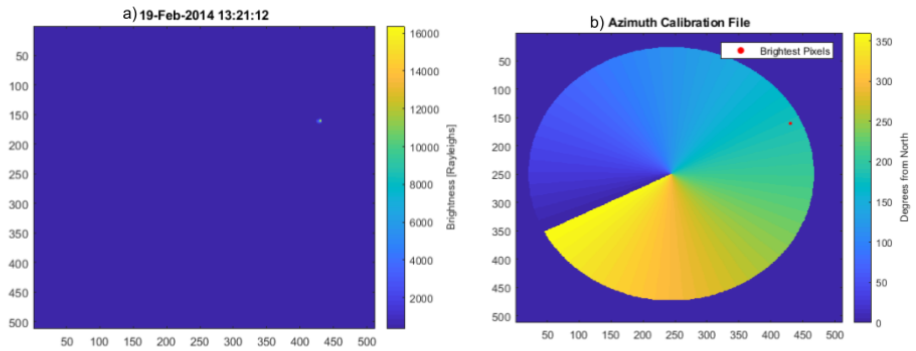

Figure 4.4. (a) Example ASI with the moon very apparent. Intensity is in kilo-Rayleighs. (b) Azimuth calibration file with the brightest pixels, the moon, of the ASI in (a) plotted.

The pixel of the moon's location is determined as the brightest pixels in the ASI. The moon pixels' row and column locations are obtained from the ASI, and the azimuth and elevation angles for those pixels are used as the moon's location. The pixel locations of the brightest pixels of the example ASI are plotted on the ASI azimuth calibration file in Fig. 4.4b. The axes are the x and y coordinates of each pixel, and the color indicates azimuth angle in degrees clockwise from north. Some of the images have multiple pixels that are at the maximum brightness for the image. In this case, the average Azimuth and Elevation values are used. The dates, times, average azimuth and average elevation values for the images that are used to check the image rotation in each year are displayed in Table 4.2.

In Stellarium, the local position is set to Poker Flat Research Range (65° 7' 32.17" N, 147° 29' 30.83" W), where the all sky images are taken. Then the date and time of ASIs where the moon is apparent are input into the program. The program then shows the sky with the celestial bodies overhead at the time input and the location selected (Poker Flat Research Range).

Selecting the moon shows a list of information, including the azimuth and elevation. These values are included in Table 4.2 along with the difference between the Stellarium values and the calibration file values. If there was an unaccounted for rotation that occurred, then there would be a major difference of the azimuth values shown in the table.

Table 4.2. Stellarium [14] and Calibration Files Moon Azimuth and Elevation Comparison.

Date	Time	Calibration		Stellarium		Difference	
[mm-dd-yy]	[UTC-0]	Az [deg]	El [deg]	Az [deg]	El [deg]	Az [deg]	El [deg]
2-19-14	13:21:12	181.75	16.00	181.77	14.67	0.02	-1.33
3-14-14	12:31:03	248.05	18.07	247.91	17.32	-0.14	-0.75
10-9-14	09:13:40	158.56	33.04	158.62	32.82	0.06	-0.22
2-23-15	06:44:21	260.38	16.60	260.24	15.50	-0.13	-1.10
2-28-15	07:11:10	203.31	40.47	203.21	40.56	-0.11	0.09
8-28-15	10:09:58	203.72	11.43	203.90	9.38	0.18	-2.05
2-13-16	07:05:09	259.79	13.77	259.66	12.30	-0.12	-1.46
3-15-16	06:57:15	240.40	31.40	240.50	31.20	0.10	-0.20
1-18-17	10:42:11	116.80	12.10	117.09	9.15	0.29	-2.95
2-27-18	04:48:02	130.03	36.28	130.13	35.77	0.10	-0.51

The table shows that there is very little difference between the ASI moon location using the calibration files and the Stellarium moon location, regardless of the year. The elevation differs by less than 3 deg, and the azimuth by less than half a degree. From this I conclude that there is no additional ASI rotation that needs to be taken into account, and any camera movement was already accounted for to match the azimuth and elevation calibration files.

4.3 Sensitivity studies

4.3.1 Magnetic Zenith Range.

The magnetic zenith limit is the maximum angular distance a satellite can be from the magnetic zenith, or up the local magnetic field line direction, for its data to be analyzed using the spectral analysis method. Fig. 4.5 shows what the magnetic zenith limit means. The cartoon on the left shows the all sky camera looking up at satellites in the sky. If the limit is set to 10 degrees for example, only satellite 1 would be analyzed and satellites 2, 3, and 4 are too far from the magnetic zenith to be analyzed. If the limit was 50 degrees, then satellites 1, 2, and 3 would be analyzed, whereas satellite 4 would be too far to be analyzed. This limit is put in place to ensure the theory that is used to determine the layer of peak ionization rate using auroral images is valid. If the satellite's angular distance from magnetic zenith is within the magnetic zenith limit, then the red-to-blue ratio can be said to correspond to the characteristic energy of the particle population. If the satellite's angular distance is outside of the magnetic zenith limit, the data is not analyzed.

The right image of Fig. 4.5 shows the red to blue ratio all sky image for march 18 and the three satellites that were in the sky sending signals that were being scintillated. The black circle outlines the 25 degree magnetic zenith limit, meaning satellites 25 and 29 would be analyzed, and satellite 31 is too far from the magnetic zenith to be analyzed.

Initially, the magnetic zenith limit was set to 25 degrees by [5]. The sensitivity of the ASI method to the magnetic zenith range is tested in this work by enforcing different limits of 5 to 50 degrees in 5-degree steps. For each limit, the number of events that are designated as E and as F are counted and the results are shown in Fig. 4.6.

Figure 4.6 plots the percent of E layer events, on the left y-axis, and the percent of F layer events, right y-axis, as the magnetic zenith limit changes. The sum of the blue and red bar adds to 100%, but the absolute number of events are

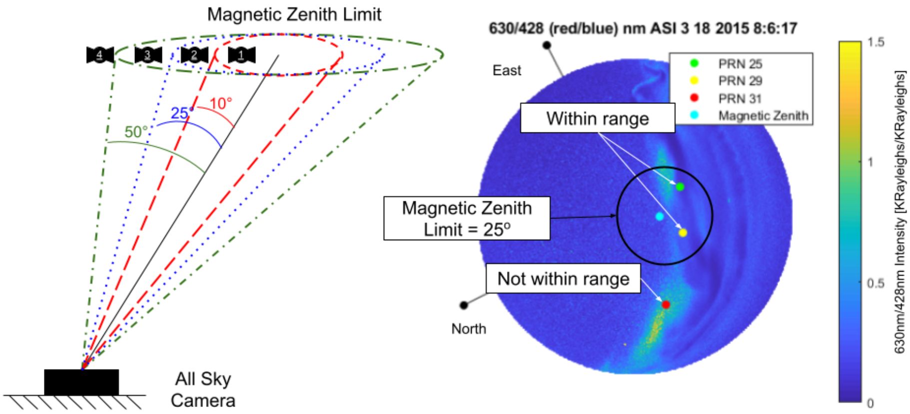

Figure 4.5. (a) A schematic explaining the magnetic zenith and how the limit determines which satellites are analyzed. (b) Red-to-blue ratio at each pixel in the all-sky image, with magnetic zenith (cyan) and scintillating satellites (green, yellow, red) marked. A circle marks the region within 25 degrees of magnetic zenith.

printed on each bar, and increase with increasing angular limit. The percents of E events (blue) and F events (red) fluctuate about 20% and 80%, respectively, by +/- 5%. This shows minor sensitivity of the spectral analysis results to the magnetic zenith limit changing. The limit that minimizes the discrepancy between the ASI and PFISR layer methods is in fact at 25°, since that is the limit that shows the highest percent of E layer results, closest to the PFISR results.

4.3.2 Number of Pixels Analyzed.

The number of pixels analyzed corresponds to how many pixels of the ASI are analyzed to determine the scintillation layer designation. In the original method [5], only the red to blue ratio of the pixel of the ASI nearest to the satellite azimuth and elevation was used. The hypothesis I test here is whether analyzing more pixels provides a better image of the characteristic energy and reduce the effect of noise or inaccuracies in satellite positiong mapping in skewing the results.

The alternate number of pixels analyzed that was tested was 9, the pixel nearest the satellite position in the sky and the 8 surrounding it. The average of the

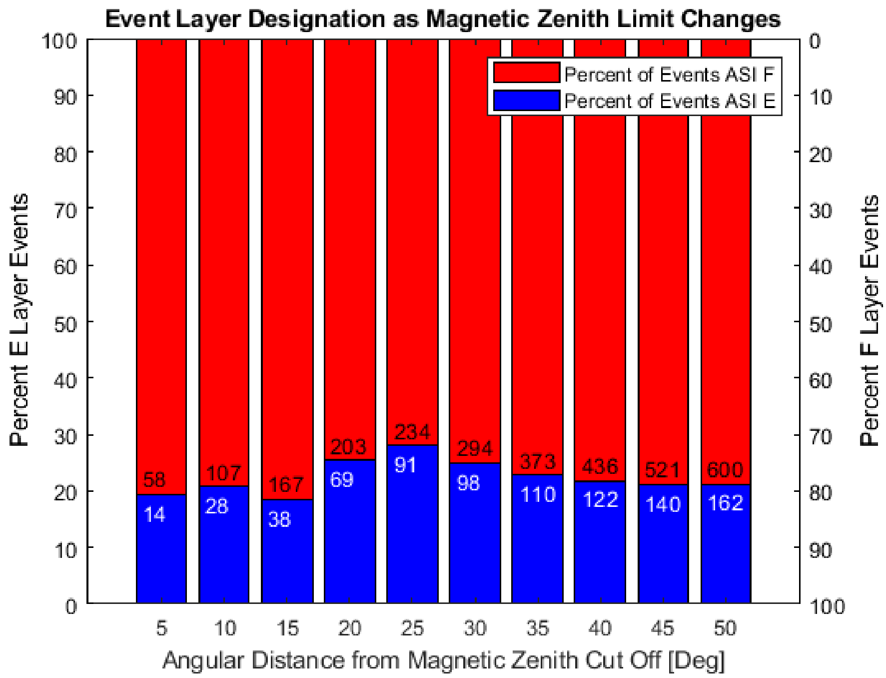

Figure 4.6. Percent of the total number of events designated as E or F layer as the magnetic zenith limit is changed. The white numbers are how many events are determined to be E layer, and the black number are how many F events there are for the corresponding magnetic zenith limit. Analysis was done using all scintillation events from 2014-2018.

red-to-blue ratio of these 9 pixels is used to categorize the scintillation event layer. These results are then compared to the original one-pixel method in Fig. 4.7 for each year.

Figure 4.7 shows a bar chart, one per year and number of pixels. For a given year, the single pixel and 9 pixel results are placed side by side. The left y axis is the percent of events that were E layer, and the right y axis is the percent of events that were F layer. The bars are red for the F layer and blue for E layer, and total 100%. The number of events classified in each layer is printed on each bar as well.

The figure shows that the number of pixels analyzed has little effect on what percent of events are E layer versus F layer. Only in the year 2014 is there any change in the number of events assigned to each layer. This indicates that the number of

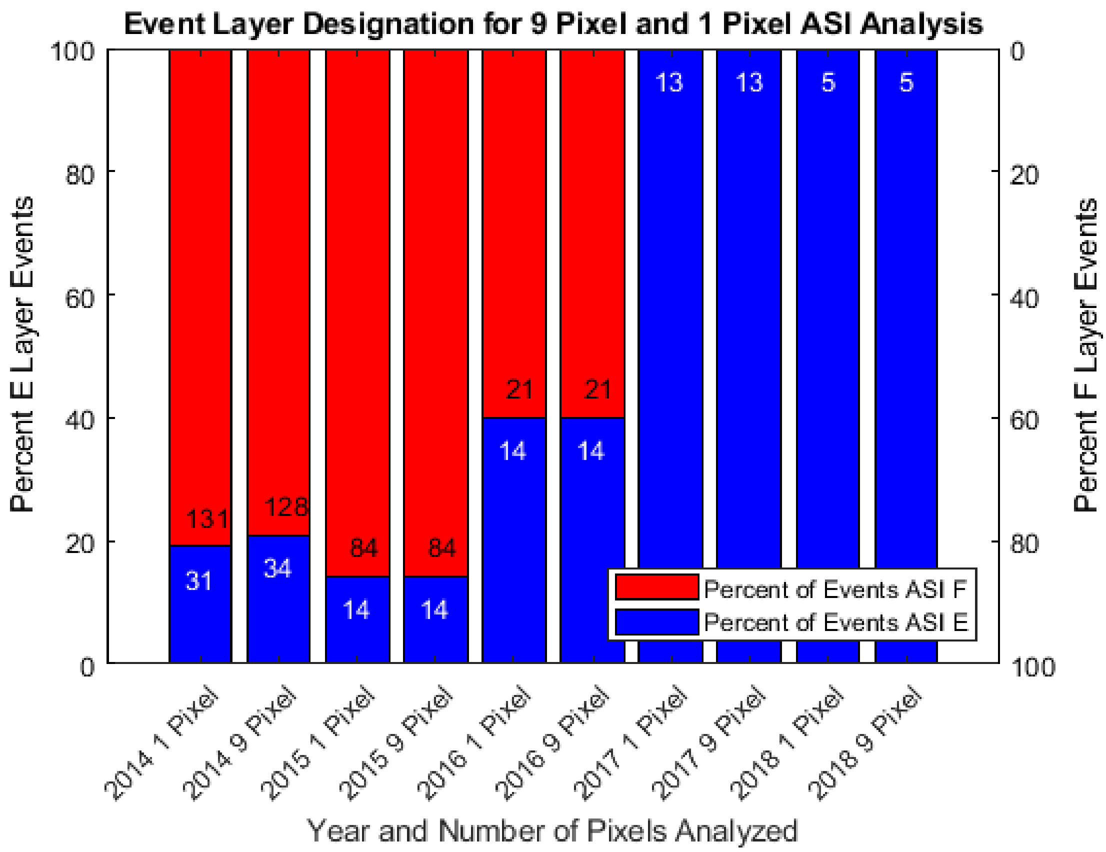

Figure 4.7. Yearly results of using 1 pixel to determine the scintillation layer vs using an average of 9 pixels. The white numbers represents the number of E layer events and the black numbers represent the number of F layer events. Analysis was done using all scintillation events in the years of 2014-2018.

pixels being analyzed has little effect on the results and may be ruled out as a possible factor in the discrepancy between layer designation via ASI versus via PFISR.

4.3.3 Time Analysis.

Time analysis refers to what portion of the entire scintillation event time is being analyzed. The spectral analysis method categorizes the events by determining the E or F layer for each 12.5-section time step (the all-sky imaging cadence) during the entire duration of the scintillation event. A majority vote was used in the original method [5] to determine the final single layer for each event. If there were more time instances during the scintillation event categorized as E, then the whole event was designated as E, and vice versa for F layer events.

The hypothesis tested here is that the layer causing the designation is best observed at some beginning fraction of the event. Then, since the lifetime of the 557 nm emission is many seconds shorter than the 630 nm emission, the irregularity layer where the scintillation actually happened gets obscured by what is observed for the rest of the event duration. If this were true, then the spectral analysis results should tend towards E if only the first portion of the event is analyzed, bringing the result into closer agreement with the PFISR layer results.

To investigate this, a time limit from the onset of scintillation is introduced. This threshold limits how much of the scintillation event duration is analyzed. For example, if the threshold is set to 30 seconds, then only the first 30 seconds of the event are analyzed to determine scintillation layer categorization. To find the optimal threshold, thresholds from 12.5 seconds to the maximum scintillation duration by 12.5 second intervals are tested. A 12.5-second start time and interval is chosen due to ASI red-blue-green image triplets being taken at 12.5 second intervals.

An example of this applied to one scintillation event is shown in Fig. 4.8. The top graph of the figures is the red-to-blue ratio from the ASIs at 12.5 s instants during the scintillation event. The middle graph shows what the E/F layer categorization is if the time threshold is set to the duration shown on the x-axis. For reference, the bottom graph shows the PFISR electron density measurements during the same scintillation event. The time of the scintillation in the PFISR graph is outlined by the vertical black lines.

The event shown in Fig. 4.8 is an example of when PFISR and ASI agreed: in both cases the layer was categorized as E. Figure 4.9 is another example investigating the time threshold, for an event in which ASI and PFISR disagree. The ASI designated the event as F layer, but PFISR designated the layer as E. We can see from the line plot of the red-to-blue ratio decision as a function of duration of time-averaging, that for nearly all time intervals, the red-to-blue ratio majority vote will return a ratio corresponding to an F layer event. The PFISR densities also seem to indicate increased F region densities within the scintillating time interval. Closer inspection of the PFISR plot shows a jump to high densities at the very lowest altitude range. For this event, it appears that the PFISR data should be investigated more closely, possibly with an inspection of the uncertainties on the PFISR measurements.

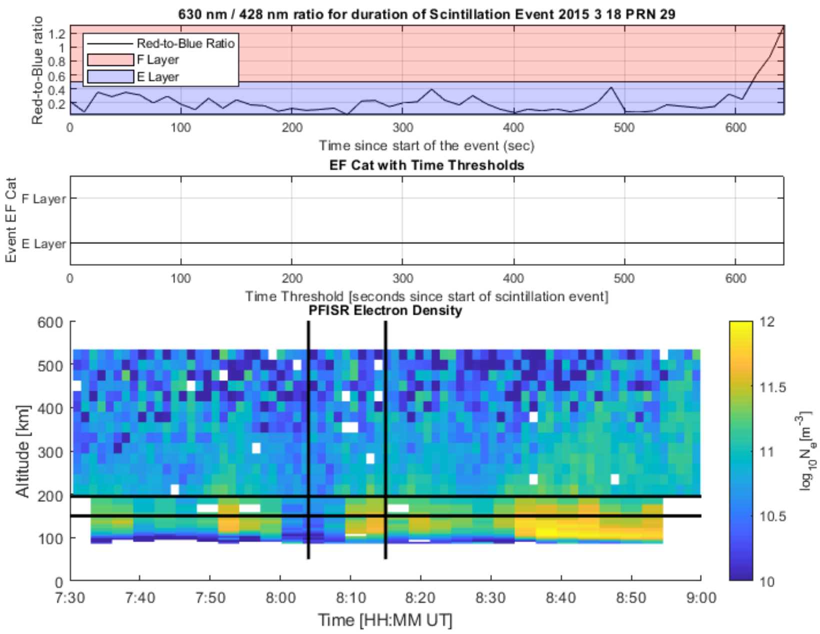

Figure 4.8. Top figure shows the red-to-blue ratio for the duration of a scintillation event on March 18, 2015, from PRN 29. The middle figure shows what the E/F layer designation would be if a total time threshold was set at each interval of the scintillation event. The bottom figure show shows the measurements from PFISR with the scintillation event duration outlined by the black vertical lines.

The method of determining what the scintillation event category would be if a time threshold is set throughout the event is applied to every event, and the total results are shown in Fig. 4.10. Figure 4.10 shows the tested time limits on the x axis, as time since the start of the scintillation event in seconds, and the percent of events

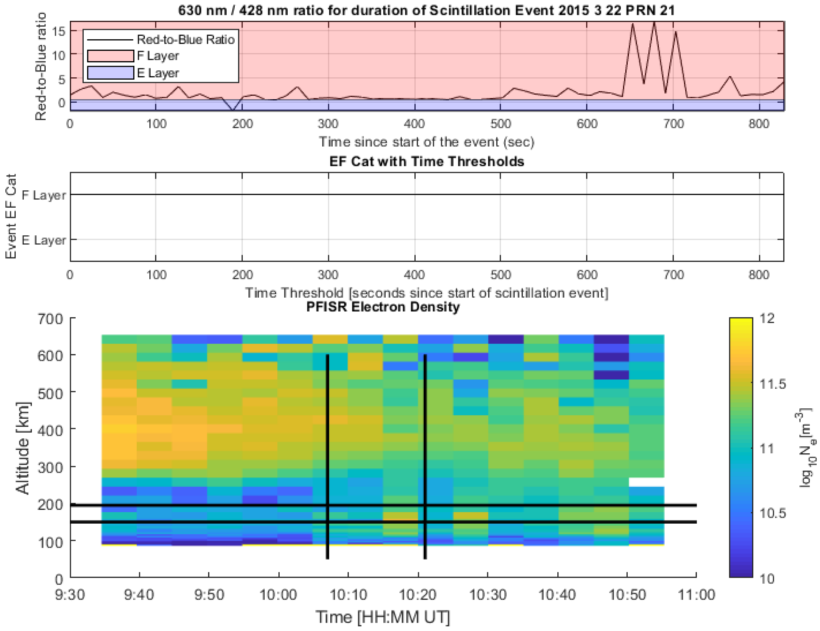

Figure 4.9. Top figure shows the red-to-blue ratio for the duration of a scintillation event on March 22, 2015, from PRN 21. The middle figure shows what the E/F layer designation would be if a total time threshold was set at each interval of the scintillation event. The bottom figure show shows the measurements from PFISR with the scintillation event duration outlined by the black vertical lines.

that would be categorized as E or F with that respective time threshold set on the y axis. If our hypothesis were correct, then there would be an increased number of E layer events with the shorter time thresholds, and the number of E events would then decrease as the threshold is increased. However, from Fig. 4.10, the opposite occurs.

4.3.4 Red to Blue Ratio Sensitivity.

The original Red to Blue (RB) ratio of 0.5 was determined to be the E/F transition energy in [15]. The RB ratio of auroral emissions corresponds to the electron characteristic energy of the emission. In our layer analysis, we assume that this corresponds to which layer of the ionosphere is experiencing the higher ionization rate.

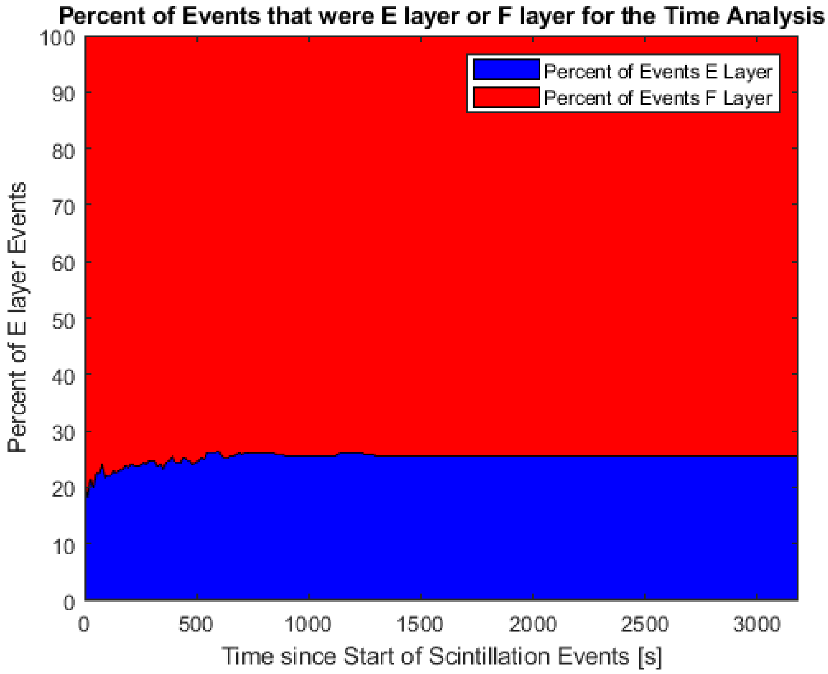

Figure 4.10. Total number of E/F layer designations average up to each duration since the start of scintillation events. Analysis was done using all scintillation events from 2014-2018.

The RB ratio is tested using detection theory, explained in Section 2.4 and applied for keogram cloud detection validation. For this investigation, PFISR is considered "truth" and the ASI spectral analysis method is considered the prediction method. The detection matrix is shown in Fig. 4.11. The optimal red to blue ratio will be the one with the least disagreement between PFISR and spectral analysis method.

RB ratio thresholds from 0.01 to 3 increased at 0.01 intervals are tested. Training data will be used to determine the optimal threshold and testing data will be used to test if the threshold found from the training data is repeatable. There are 176 events from 2014-2018 where there is both a PFISR layer designation and an ASI layer designation. The training data consist of 88 of these events and the testing data consist of 82 of the events. The data is separated into these two sets by alternately assigning each event in the set of 176 as "training" or "testing" events.

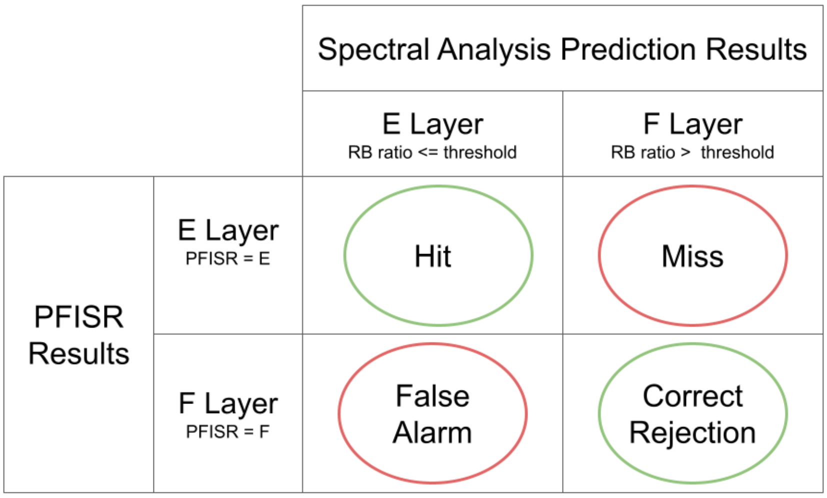

Figure 4.11. Detection Theory used to determine the optimal red to blue ratio.

To determine the ideal threshold using the training data, each threshold from 0.01 to 3 by 0.01 is looped through and the ASI scintillation layer is categorized using the RB ratio and the RB threshold, in the same way as the original method. Then the results are compared against PFISR designations using detection theory and the ideal threshold is found. The ideal threshold is then applied to the testing data to determine the repeatability.

Figure 4.12 shows the results of determining the ideal threshold (x-axis) plotting the percent of events that PFISR and ASI disagreed (y-axis) for each tested threshold, using the training data. The threshold with the lowest percent of disagreements is 1.43 with a mislabeling rate of 19.51%. For comparison, the original threshold of 0.5 on the training data produces a disagreement rate of 45.45%.

Applying the ideal threshold of 1.43 to the testing data produces a disagreement of 19.32%, whereas using the original threshold of 0.5 on the testing data produces a disagreement of 59.75%. Using the ideal threshold on the testing data produces results similar to the training data, meaning the threshold is consistent when used on multiple data sets. This brings up the question: why does the spectral anal-

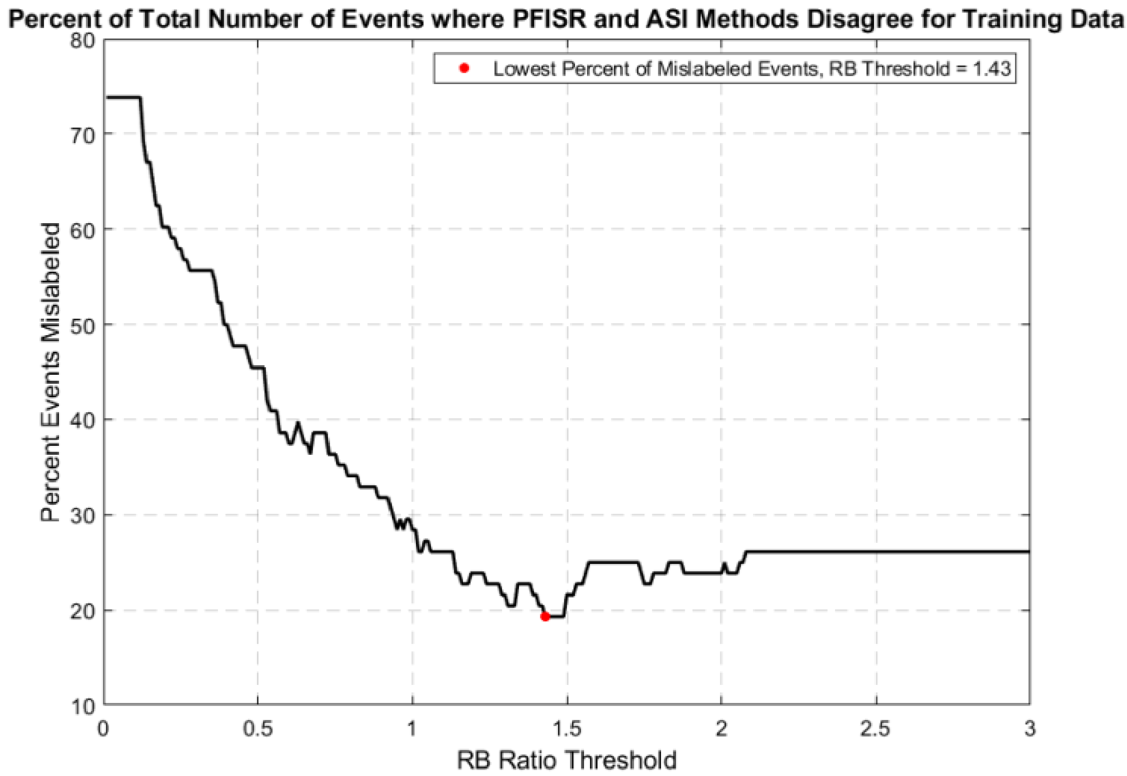

Figure 4.12. Results of testing RB ratio thresholds 0.01 to 3 by steps of 0.01 on the training data.

ysis method have an ideal E/F region cutoff at 1.43 when previous literature shows that 0.5 is the threshold? This is discussed further in Chapter 5.

4.4 All Sky Image Analysis Results

After further investigation into the ASI spectral analysis method, it was found that the method was only sensitive to changing the red to blue ratio threshold. This new threshold is not implemented into the ASI spectral analysis method as more research into the underlying assumptions is needed before making such a change. Another possible way of investigating this is discussed in Section 5.2.

The keogram cloud detection method was improved by making the flat field gain calculation more automated. The study was also expanded from the original 2014-2015 run to 2014-2018. The results of running the ASI method with the improved cloud detection method implemented are summarized in Fig. 4.13.

The results aren't broken down by year as in Table 2.1, rather the results are the total for each year organized by the scintillation category. The categories are organized first by the scintillation type: SP for phase scintillation, S4 for amplitude scintillation, SPS4 for phase and amplitude scintillation. The results are further subdivided by the frequency of the signal: L1CA (1575.42 MHz) and L2CL (1227.60 MHz). Categorizing in this way creates six unique categories, as seen in the scintillation category column.

The total scintillation events column lists the total number of events recorded from 2014 to 2018 for the respective scintillation categories. The next column shows how many of those events occur at night and have keograms available during the scintillation event. The percentage is listed below the total number. Then, the number of events that have aurora present is listed, with the percentage of the set having keograms available listed underneath. The next column identifies how many events are cloud-free using the improved cloud detection method. Then, of those cloud-free events, the number of events that are within 25° of the magnetic zenith are listed. The final number of events that are near the magnetic zenith are the events that are used in the ASI spectral analysis method to determine the scintillation event layer.

The next three columns show how the event layer categorizations are distributed, the first two being E and F layer. The percent of E and F layer events are computed with respect to the number of events near the magnetic zenith. The "no designation" column are the number of events from the initial set of scintillation events that were not analyzed due to one the criteria not being met, with the percentage listed with respect to the total number of scintillation events (column 2).

The last set of columns are the results from PFISR layer designation, for comparison. The columns for E and F layer are event layer categorizations. The events that are "ambiguous" did have data but the layer could not be determined from the PFISR data [12], and the "no data" events didn't have any PFISR data available [7]. The percentages are computed with respect to the total number of events (column 2). The table in Fig. 4.13 shows that most of the events that were recorded were phase scintillation events of the L1 frequency. The final row, the total, is the sum of all the scintillation category results.

The final results show that the ASI method still gives a majority of events as F layer, at a rate of 3 F layer events for every 1 E layer event. The PFISR method shows a majority of the events for which a layer can be designated are E layer, at a rate of about 4-to-1 E-to-F (see 40% E layer to 11% F layer in the "Total" row).

A more direct comparison of the PFISR and ASI results is given in the table in Fig. 4.14. The table in Fig. 4.14 shows that, of the events that have both ASI and PFISR designations, how many of the events were categorized: both E layer; both F layer; E layer ASI and F layer PFISR; and F layer ASI and E layer PFISR. Of the 176 events, for 46.8% of the events PFISR and ASI agree, but the other 53.4% of the events, ASI categorized as F layer and PFISR categorized as E layer. This shows a major skew in one direction.

This skew of the results lines up with the optimal red to blue ratio being found as 1.43. Before implementing the new 1.43 red to blue ratio, more research needs to go into how comparable the two methods are. It is possible that a least a few of the events that are designated by PFISR as E layer, such as the one shown in Fig. 4.9, might be due to data uncertainties in PFISR, which were not taken into account in the method of [12] that were applied in producing the event database this work uses from [7]. But it remains to be seen whether PFISR data quality as quantified by uncertainties would account for all 50% of the events for which PFISR determines an event as E layer but ASI as F layer.

Scintillation Category	Number of Scintillation Events	Subset At Night with Keograms Avaliable	Subset with Aurora Present	Subset Cloud-free	Subset Near Magnetic Zenith	ASI E Layer	ASI F Layer	ASI No Designation	PFISR E Layer	PFISR F Layer	PFISR Ambiguous Layer	PFISR No Data
Total SP L1CA	2766	1249	1187	759	206	55	151	2560	1096	296	285	1089
		45.16%	95.04%	63.94%	27.14%	26.70%	73.30%	92.55%	39.62%	10.70%	10.30%	39.37%
Total SP L2CL	1628	748	701	449	108	25	83	1520	686	196	140	606
		45.95%	93.72%	64.05%	24.05%	23.15%	76.85%	93.37%	42.14%	12.04%	8.60%	37.22%
Total S4 L1CA	2	0	0	0	0	0	0	2	0	1	0	1
		0%	0%	0%	0%	0%	0%	100%	0%	50%	0%	50%
Total S4 L2CL	11	3	3	1	0	0	0	11	1	9	0	1
		27.27%	100%	33.33%	0%	0%	0%	100%	9.09%	81.82%	0%	9.09%
Total SPS4 L1CA	6	0	0	0	0	0	0	6	0	4	0	2
		0%	0%	0%	0%	0%	0%	100%	0%	66.67%	0%	33.33%
Total SPS4 L2CL	11	2	2	2	2	0	2	9	0	10	1	0
		18.18%	100%	100%	100%	0%	100%	81.82%	0%	90.91%	9.09%	0%
Total	4424	2002	1893	1211	316	80	236	4108	1783	516	426	1699
		45.25%	94.56%	63.97%	26.09%	25.32%	74.68%	92.86%	40.30%	11.66%	9.63%	38.40%

Figure 4.13. Results after running ASI spectral analysis using the new cloud detection method and dark sky cut off.

Total Events = 176 Layer Designation		PFISR	
		E	F
ASI	E	41	0
	Percent	23.29%	0%
	F	94	41
	Percent	53.40%	23.29%

Figure 4.14. Comparing ASI spectral analysis results with the PFISR results for the 176 events that can be used for both an ASI and PFISR layer designation with the red to blue ratio threshold set to 0.5.

CHAPTER 5

CONCLUSION

5.1 Summary

A previously developed method [5] to detect clouds using keograms and then determine scintillation event layer using optical all sky images was found to give very different scintillation event layer results from those of a radar-based method [7]. These original results of ASI scintillation event categorization and the comparison to PFISR are shown in Table 2.1. These results showed that there was a major disagreement between the two methods. The ASI method was determining that most of the events were occurring in the F layer, whereas PFISR was determining that most of the events were occurring in the E layer. Possible reasons for this disagreement was investigated in this thesis.

The first question was whether there was an error with the ASI spectral analysis algorithm. The first part of the algorithm was the keogram analysis for cloud detection. The keogram analysis method was improved by creating a more automated method of calculating the flat field gain, finding a flat field gain for each year rather than just using a single year and day flat field gain for the entire study, and validating the cloud detection method using NOAA cloud mask data. As a result of the validation, I determined that the optimal 557 nm coefficient of variation threshold was 0.37, with a 22.4% of mislabeled events on the odd year set of data and a 24% of mislabeled events when being tested on the odd year set of data.

The second part of the algorithm analyzes the ASIs during cloud-free periods to determine the scintillation event layer. During this process, there were a few constants and thresholds that were set in the original version of the method that I investigated further to see if the resulting layers were sensitive to changing any of these parameters. If the final results were sensitive to any of these thresholds, the cause for this would have also been investigated further.

I checked that the azimuth/elevation calibration files for the ASIs were valid for all years. After checking the calibration file against independent calculations of the position of the moon with astronomical software Stellarium, I found that the file was true for all years 2014-2018. This ruled out pixel viewing angle mapping errors as a possibility as to why layers might disagree, and why the percent of events near the magnetic zenith decreased from year to year.

In the ASI sensitivity study section, the range of the magnetic zenith limit, the number of ASI pixels analyzed, and the portion of the scintillation event time were analyzed and found to have little to no effect on the layer categorization results. The red-to-blue ratio that used for deciding the scintillation event layer was analyzed, and changing that had a major effect on the results. Using training data, it was found that the ideal threshold was 1.43, with a misdetection rate of 19%. This threshold has not yet been implemented into the method. The sample size of the study was relatively small, with 176 total events for which both PFISR and ASI designate a layer for a scintillation event. Additionally, the scintillation list only provides the overall PFISR layer designation. As with the ASI method, there is a layer designation for every time point during the PFISR algorithm, but it also uses a majority rule to give the final result. This means each red-to-blue ratio for the entire event is being compared to only one PFISR layer designation, when in reality each individual time point has its own PFISR designation. In the future, it would be useful to get the PFISR results for each individual time point and then compare them to their corresponding ASI red-to-blue ratios. This might give a better result when trying to further resolve the discrepancy.

This in-depth study shows that the discrepancy between the ASI spectral analysis method and PFISR result is most likely due to the fundamental differences between the two methods, rather than flaws within the ASI method. More work needs to be done to determine how ASI and PFISR can be correlated and which method might be more correct in determining the scintillation event layer.

5.2 Future Work

After further investigation into the spectral analysis method, there is still a major discrepancy between the ASI and PFISR methods. The methods are fundamentally different. PFISR measures the electron density, and the ASI method measures the ionization rate, the production rate of electrons. It is possible that the methods will never agree. It is also possible that the red-to-blue ratio, which relies on an assumption of a Maxwellian particle population, does not hold for some scintillation events, such that the ratio does not give a meaningful indication of the ionization rate as a function of height.

To further analyze how comparable the methods are, it would be useful to calculate the precipitating fluxes from the ASI color ratios and separately using PFISR, to see how those results compare. This gives a method of directly comparing both methods to see whether and how much they align. Also, repeating the red to blue ratio threshold analysis but comparing each time step of the PFISR and ASI methods and using the ASI pixel at the PFISR beam instead of the satellite that is producing the scintillating signal might help clarify the reason for the disagreement.

The coefficient of variation is a good metric for determining cloudy and cloud-free sky using keograms. Using the method on keograms is a very computationally time efficient way of determining cloud cover. To get a more accurate cloud cover analysis, it might be possible to use the coefficient of variation on the ASI to determine which portions of the ASI are cloudy.

It could also be that the method of the ASI layer and PFISR layer determination are not optimal, but only proxies for identifying the irregularity layer. Scintillation events are caused by a sudden variation in the plasma density spatially. Instead of finding the layer with the peak density or ionization rate, it might be more accurate to determine the scintillation event layer as the layer with the most sudden electron density or ionization rate change.

BIBLIOGRAPHY

[1] T. F. Tascione, *Introduction to the Space Environment, 2nd ed.* Malabar, Florida: Krieger Publishing Company, 1994.

[2] E. Petrie, M. Pajares, P. Spalla, P. Moore, and M. King, "A review of higher order ionospheric refraction effects on dual frequency GPS," *Surv. Geophys.*, vol. 32, pp. 197–253, 05 2011.

[3] K. C. Yeh and C.-H. Liu, "Radio wave scintillations in the ionosphere," *Proceedings of the IEEE*, vol. 70, p. 324–360, Apr 1982.

[4] D. Hampton, "Archive data." http://optics.gi.alaska.edu/optics/archive. Accessed: 19-Apr-2020.

[5] D. Stuart, "Multiyear automated analysis of auroral images to categorize ionosphere irregularity layer," Master's thesis, Illinois Institute of Technology, Chicago, IL, May 2020.

[6] Y. Su, S. Datta-Barua, G. S. Bust, and K. B. Deshpande, "Distributed sensing of ionospheric irregularities with a gnss receiver array," *Radio Science*, vol. 52, no. 8, p. 988–1003, 2017.

[7] S. Datta-Barua, P. Llado Prat, and D. L. Hampton, "Multiyear detection, classification and hypothesis of ionospheric layer causing gnss scintillation," *Radio Science*, vol. 56, no. 12, 2021.

[8] H. Abdi, "Signal detection theory," *International Encyclopedia of Education*, p. 407–410, 2010.

[9] U.S. Coast Guard Navigation Center, "GPS almanacs, nanus, and OPS advisories archives." https://www.navcen.uscg.gov/?Do=gpsArchives. Accessed: 18-Apr-2020.

[10] M. H. Rees and D. Luckey, "Auroral electron energy derived from ratio of spectroscopic emissions 1. model computations," *Journal of Geophysical Research*, vol. 79, no. 34, p. 5181–5186, 1974.

[11] National Oceanic and Atmospheric Administration, "AVHRR + HIRS cloud properties - PATMOS-x CDR." https://www.ncei.noaa.gov/products/climate-data-records/avhrr-hirs-cloud-properties-patmos (accessed: 04.16.2022).

[12] V. Sreenivash, Y. Su, and S. Datta-Barua, "Automated ionospheric scattering layer hypothesis generation for detected and classified auroral global positioning system scintillation events," *Radio Science*, vol. 55, no. 1, 2020.

[13] D. Hampton, "Keogram 15 hr summaries." http://optics.gi.alaska.edu/real time/data/PKR_DMSP/Keo_15hr/Keo_15hr/2019/ (Accessed: 11.23.22).

[14] G. Zotti, S. M. Hoffmann, A. Wolf, F. Chéreau, and G. Chéreau, "The simulated sky: Stellarium for cultural astronomy research," *Journal of Skyscape Archaeology*, vol. 6, p. 221–258, Mar. 2021.

[15] P. M. Banks, C. R. Chappell, and A. F. Nagy, "A new model for the interaction of auroral electrons with the atmosphere: Spectral degradation, backscatter, optical emission, and ionization," *Journal of Geophysical Research*, vol. 79, no. 10, p. 1459–1470, 1974.